


## Article

# Geochemical and Isotopic Compositions of Fluorites from the Yama Fluorite Deposit in the Qilian Orogen in Northwest China, and Their Metallogenic Implications

He Jiao <sup>1</sup>, Guo-Biao Huang <sup>1</sup>, Wei Ma <sup>1</sup>, Qiang-Qiang Cui <sup>1</sup>, Wei-Hu Wang <sup>1</sup>, Qing-Feng Ding <sup>2,\*</sup> , Xuan Zhou <sup>2</sup> and Rui-Zhe Wu <sup>2</sup>

<sup>1</sup> Qinghai Provincial Key Laboratory of Salt Lake Resources Exploration and Research in Qaidam Basin, Qaidam Integrated Geological Exploration Institute of Qinghai Province, Golmud 816099, China; jiaofushun666@163.com (H.J.); hsy20200205@163.com (G.-B.H.); 13369796086@163.com (W.M.); zailushang1215@163.com (Q.-Q.C.); hu861025.cool@163.com (W.-H.W.)

<sup>2</sup> College of Earth Sciences, Jilin University, Changchun 130061, China; xuanzhou21@mails.jlu.edu.cn (X.Z.); rzwu22@mails.jlu.edu.cn (R.-Z.W.)

\* Correspondence: dingqf@jlu.edu.cn

**Abstract:** The Yama area is characterized by numerous large-scale fluorite–quartz veins that are located along faults within the widespread Late Devonian–Late Silurian syenogranites in the Tataleng granitic batholith, Qilian Orogen, Northwest China. These fluorite–quartz veins contribute to an important fluorite reserve, but their ore genesis remains unresolved so far. In this study, trace elements, rare earth elements (REEs), and hydrogen, oxygen, and strontium isotopic compositions of fluorites are analyzed. The studied fluorite samples have similar chondrite-normalized REEs, including Y patterns, with relatively strong enrichment in heavy REEs, negative Eu anomalies, strongly positive Y anomalies, and comparably invariable Y/Ho ratios of 41.43–73.79, suggesting a unique hydrothermal genesis. The relatively variable values of  $\delta D$  and  $\delta^{18}O$  are  $-77.4\text{‰}$  to  $-102.4\text{‰}$  and  $-12.7\text{‰}$  to  $-4.3\text{‰}$ , respectively, close to the meteoric water line. These fluorites yield relatively invariable analytical  $^{87}Sr/^{86}Sr$  ratios of 0.749089–0.756628 (except for an anomalously high ratio), and their calculated initial  $^{87}Sr/^{86}Sr$  ratios, based on the ore-forming ages provided, are apparently higher than the calculated initial  $^{87}Sr/^{86}Sr$  ratios of syenogranite wall rocks. Collectively, the geochemistry of trace elements, REEs, and stable isotopes (H, O, and Sr) suggests that the ore-forming fluids were of meteoric origin and that the Sr sources were directly derived from the ore-forming fluids themselves rather than syenogranite wall rocks. Finally, it was considered that the Yama fluorite deposit is a fault-controlled hydrothermal vein-type deposit which was possibly related to the evolution of the Paleo-Tethys Ocean in the Permian–Triassic.

**Keywords:** H–O isotope; Sr isotope; trace and rare earth elements; ore genesis; fluorites



**Citation:** Jiao, H.; Huang, G.-B.; Ma, W.; Cui, Q.-Q.; Wang, W.-H.; Ding, Q.-F.; Zhou, X.; Wu, R.-Z.

Geochemical and Isotopic Compositions of Fluorites from the Yama Fluorite Deposit in the Qilian Orogen in Northwest China, and Their Metallogenic Implications. *Minerals* **2024**, *14*, 37. <https://doi.org/10.3390/min14010037>

Academic Editor: Maria Economou-Eliopoulos

Received: 1 December 2023

Revised: 26 December 2023

Accepted: 27 December 2023

Published: 28 December 2023



**Copyright:** © 2023 by the authors. Licensee MDPI, Basel, Switzerland. This article is an open access article distributed under the terms and conditions of the Creative Commons Attribution (CC BY) license (<https://creativecommons.org/licenses/by/4.0/>).

## 1. Introduction

The Qilian Orogen (QLO) is traditionally subdivided from north to south into the North Qilian Belt (NQB), the Central Qilian Block (CQB), and the South Qilian Belt (SQB) (Figure 1a) [1–6]. It is generally believed that the QLO has developed as a result of the closure of the Proto-Tethys Ocean [1,2,6–10]. Because numerous granitic rocks in the QLO are thought to be associated with subducted, collisional, or post-collisional magmatism that was connected to the Proto-Tethys Ocean, these rocks have been studied in the past [1,4,6,10–20]. Following the widespread Early Paleozoic granitic magmatism, numerous hydrothermal mineralizations of W, Mo, Nb, Ta, Cu, Pb, Zn, Au, and F have been developed throughout the NQB and CQB [6,21–23]. However, in the SQB, there are apparently less granitic-magmatism-related mineralizations than those in the NQB and CQB. Currently, the SQB has only a limited number of significant mineral deposits,

including a few gold deposits in the Danghe Nanshan mountain in the northern margin of the SQB [6,21], a few W deposits in the Tianjun area in the central segment of the SQB [6,23], and the Yama fluorite deposit and the Yansenhada (i.e., Yamatu) quartz vein deposit in the Tataleng granitic batholith in the western segment of the SQB [6,10,23,24]. Any detailed reports of geological and geochemical research on the mineralization in the SQB are lacking, leaving the ore genesis unresolved for the time being. Specifically, there are no reports on the geological and geochemical characteristics, the ore-forming age, and the ore genesis of the Yama fluorite deposit. Furthermore, in order to assess more accurately the potential for mineralization in the granitic rocks located in and around the Yama fluorite deposit within the Tataleng granitic batholith, it is necessary to conduct detailed geological and geochemical research on this fluorite mineralization.

This paper presents the trace elements and REE abundance, as well as the H, O, and Sr isotopic compositions of fluorites from various types of fluorite ores in the Yama fluorite deposit within the Tataleng granitic batholith in the SQB. The aim is to investigate the ore-forming fluid origin, metallogenic source, and ore genesis of the fluorite–quartz veins in the Yama area as well as the potential fluorite mineralization of syenogranites within the Tataleng granitic batholith.

## 2. Geological Background and Geology of the Yama Fluorite Deposit

### 2.1. Geological Background

The Qinghai–Tibet Plateau’s northeastern edge hosts the QLO, which is bordered by the Alxa Block to the north and the Quanji massif (QM) to the south (Figure 1a) [4,6]. The QLO, the northernmost orogenic collage of the Tethyan domain, has an excellent record of the Early to Middle Paleozoic subduction–accretion that resulted from the convergence of the Alax and Qaidam blocks [1,6,9,25]. The North Qilian and South Qilian suture zones normally split the OLO into three tectonic belts, i.e., the NQB, CQB, and SQB (Figure 1a) [1,3,4,6,7,9,10,26].

The NQB is widely recognized as a typical cold oceanic suture zone resulting from the closure of the Early Paleozoic North Qilian Ocean along the North Qilian suture zone [1,2,4,6,18,27]. It hosts Early Paleozoic ophiolite sequences (560–450 Ma), high-pressure metamorphic belts, island-arc-related volcanic rocks (510–450 Ma), and granitic intrusions or plutons (510–420 Ma), as well as Silurian flysch formations, Devonian molasses, and Carboniferous to Triassic sedimentary cover sequences [2–4,6,20,27,28]. The CQB has been previously considered as either a detached fragment of the Yangtze Craton [3,6,20,29], a fragment rifted from the Alxa Block [2,4,6,30,31], or a fragment of an accretionary orogen [1,6]. Within the CQB, numerous Precambrian rocks, Cambrian to Ordovician volcanic sequences, Paleozoic sedimentary sequences, and Early Paleozoic granites have been identified [4,6,28,31]. The SQB is generally considered to be an accretionary belt comprising microcontinents, ophiolite complexes, and Early Paleozoic arc-related magmatic rocks [1,5,6,20,25]. The Early Paleozoic arc-related magmatic rocks in the SQB are mainly composed of dominant granitic rocks including several large-scale granitic batholiths, such as the Tataleng granitic batholith [6,10,11,20,32–37], the Delingha pluton [18], and the Huangyuan pluton [38]. These granitic rocks from the Early Paleozoic era are typically believed to have formed due to subduction and collisional events related to the South Qilian Ocean, which was a southern branch of the Proto-Tethys Ocean in the Qilian Orogen [14,17–20]. The Yama fluorite deposit is situated in the eastern section of the extensive Tataleng granitic batholith (Figure 2).

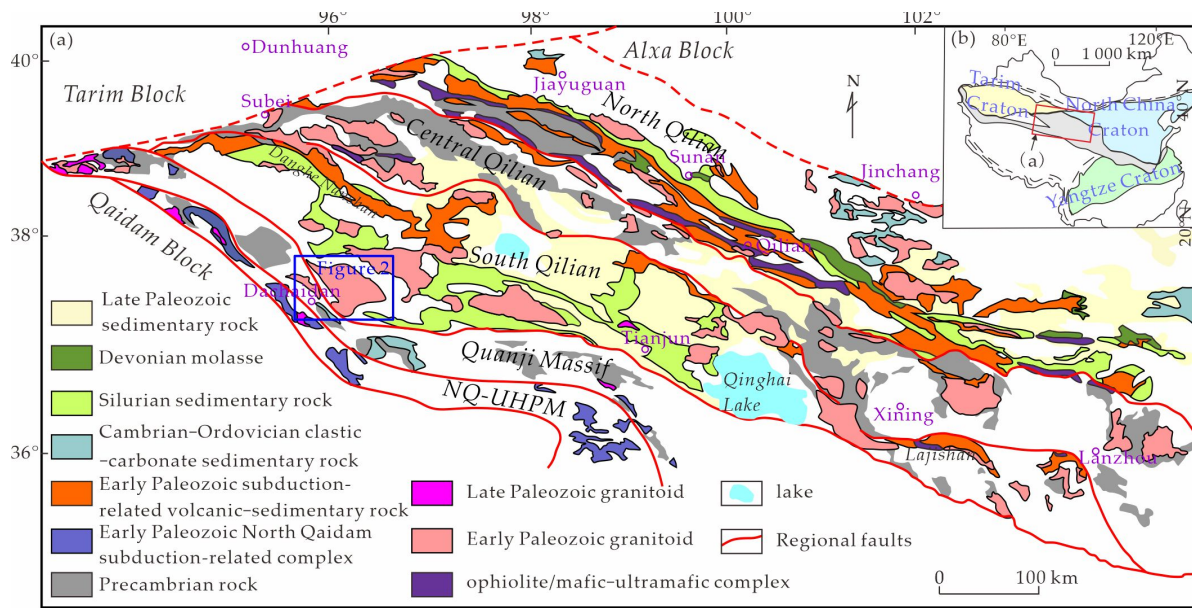


**Figure 1.** (a) Regional geological map of the Qilian Orogen (revised after [4]). NQ-UHPM (North Qaidam-ultrahigh-pressure metamorphic belt). (b) Schematic map showing major tectonic units in China (simplified after [39]).

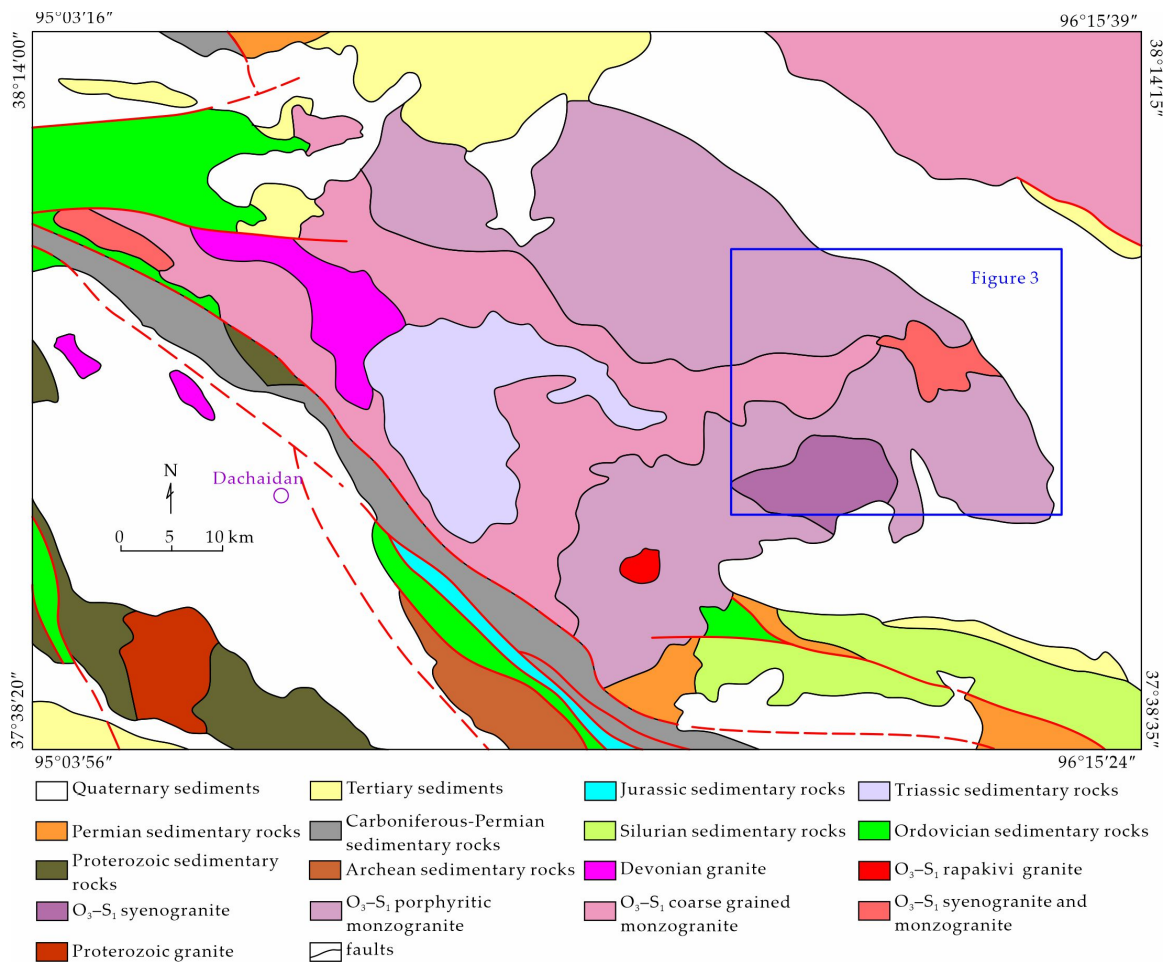


**Figure 2.** Geological map of the Tataleng granite batholith in the Southern Qilian Belt revised by [24]. O<sub>3</sub>-S<sub>1</sub>: the Late Ordovician to Early Silurian.

## 2.2. Geology of the Yama Fluorite Deposit

The Tataleng granitic batholith is situated in the northwestern part of the SQB (Figure 2) [10,20]. Quaternary sediments cover the northern, eastern, and southeastern regions of the Tataleng granitic batholith, while its southwest edge is adjacent to northwest-striking ductile faults with the Carboniferous to Permian sedimentary rocks (Figure 2). The Tataleng granitic batholith underwent a long crystallization period, ranging from the Late Ordovician to the Early Silurian ( $O_3-S_1$ ) [10,20,24,32,34,35,37,40,41]. The central part of the Tataleng granitic batholith is covered by Triassic sedimentary rocks (Figure 2) [20].

The Yama fluorite deposit is situated in the eastern section of the Tataleng granitic batholith. Throughout the study region, the  $O_3-S_1$  granitic rock outcrops are widely exposed, with the exception of the southeast part which is extensively covered by massive Quaternary sediments (Figure 3) [10,24]. Numerous northeast-striking faults and minor northwest-striking faults have developed in the  $O_3-S_1$  syenogranites. Numerous fluorite-free quartz veins and fluorite-quartz veins were emplaced along these faults within the  $O_3-S_1$  syenogranite in the Yama area (Figure 3) [10,24]. Fluorites are of high economic significance due to their abundance in numerous large-scale fluorite-quartz, of which 81 fluorite ore bodies or fluorite mineralized occurrences, ranging from No. M1 to No. M81, has been delineated in the Yama area. Among 81 fluorite ore bodies or fluorite mineralized occurrences, 76 fluorite ore bodies contribute to an important, inferred 3,555,500 tons fluorite reserve at 34.53% grade in the Yama fluorite deposit [24], in which the No. M23 fluorite ore body yield inferred a 1,844,400 tons fluorite reserve at 37.38% grade. Most of the fluorite ore bodies are located in the Yama ore district (Figure 4a), except ore body M33 which is located in the Wulandawu ore district (Figure 4b). The Yama porphyritic syenogranite, located in the central part of the Yama area, and the Wulandawu syenogranite, located in the northwest of the Yama area, make up the wall rocks of the fluorite-quartz veins in the Yama fluorite deposit (Figure 3) [10].

Based on the geological relationship (Figure 5), it can be observed that generally the fluorite-free quartz veins were formed earlier than the fluorite-quartz veins, and then a few quartz-calcite veinlets can be seen cutting the fluorite-quartz veins. Additionally, the paragenetic sequences for the Yama fluorite mineralization can be divided into two major stages, i.e., the pre-ore quartz stage and the ore-forming hydrothermal stage, and the latter stage could be subdivided into the quartz-fluorite epoch and the quartz-calcite epoch (Figure 6). Fluorite-free quartz veins, fluorite-quartz veins, and a few quartz-calcite veins were also formed in the pre-ore stage, the quartz-fluorite epoch, and the quartz-calcite epoch, respectively.

Fluorite ore bodies are commonly located within fluorite-quartz veins, which strike predominantly north-northwest (NNW), with minor northeast (NE) or north (Figure 4), and they dip predominantly in the NE (Figure 5). Rare alterations can be observed close to fluorite-quartz veins within the syenogranite wall rocks. The fluorite ore bodies are usually continuous in striking length from 67 m to 1200 m and are generally invariable in width from 0.72 to 7.3 m. A few of them have branches and variable widths in single veins (Figures 4 and 5). Fluorite-quartz veins are generally characterized by vein structures (Figure 7a,d,g), and some narrow quartz-fluorite veins intruded into brecciated syenogranite wall rocks, showing veinlets, stringer structures (Figure 7d), and/or pectinate (where the quartz is vertical to the margin of veins, Figure 7g-i); herein, we named these fluorite ores as Type 1. Type 1 ores commonly consist of fluorite and quartz, with minor quantities of sericite and calcite (Figure 7). However, some important fluorite-quartz veins may also enclose certain variable sizes of wall rock breccias, showing breccia structures within the veins (Figure 7j,m,n); herein, we named these fluorite ores as Type 2. Breccias in Type 2 ores should be derived from variable numbers and sizes of syenogranite wall rocks (Figure 7j,m), and the fine-grained fluorites and quartz which commonly grow around syenogranite breccias show crusty or colloform structures (Figure 7l,n,o), indicating such fluorites might be crystallized earlier than those in Type 2 ores during a low-temperature mineralization process.



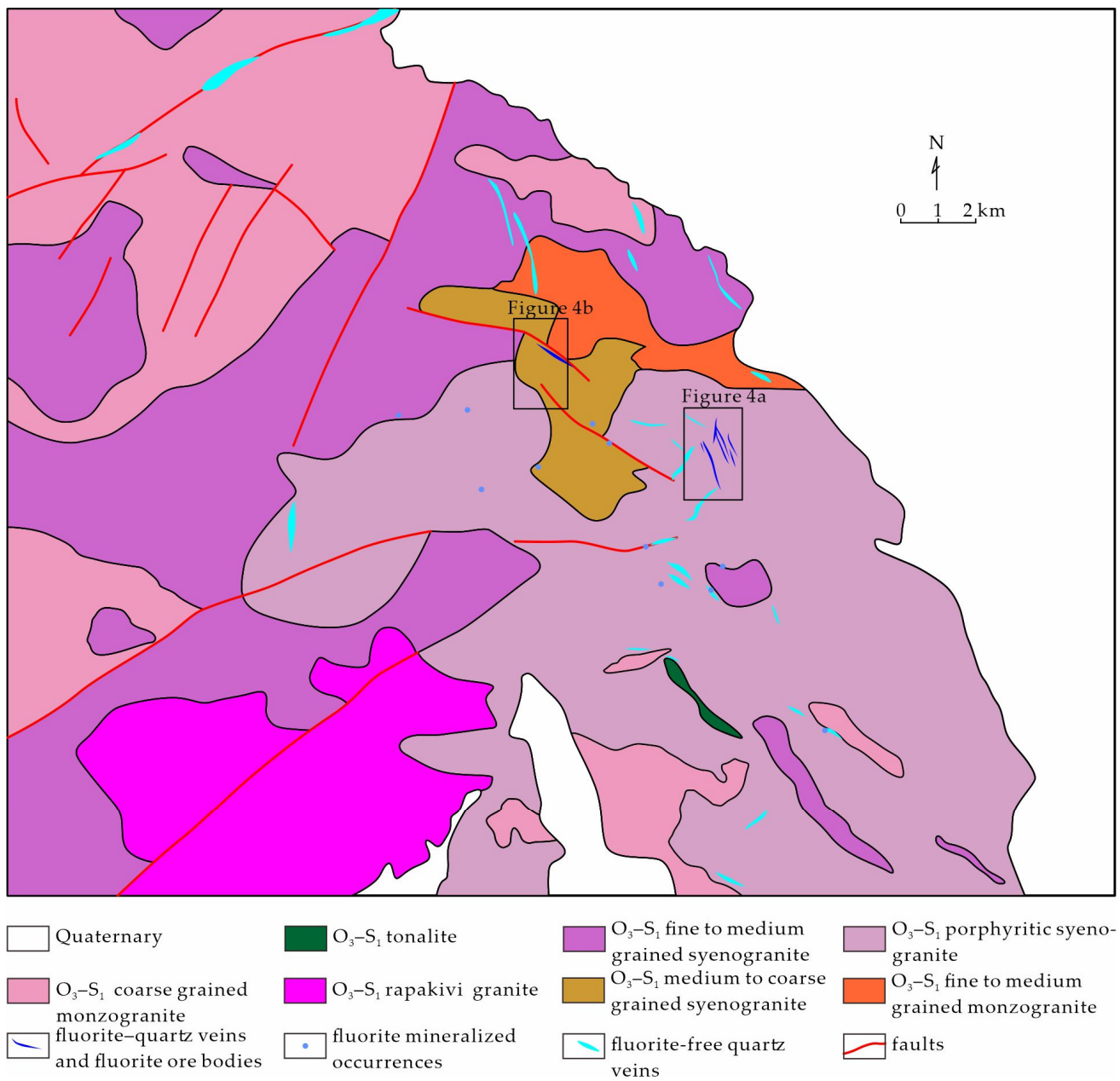


**Figure 3.** Geological map of the Yama fluorite deposit in the Eastern segment of the Tataleng granitic batholith (revised after [24]). O<sub>3</sub>-S<sub>1</sub>: the Late Ordovician to Early Silurian.

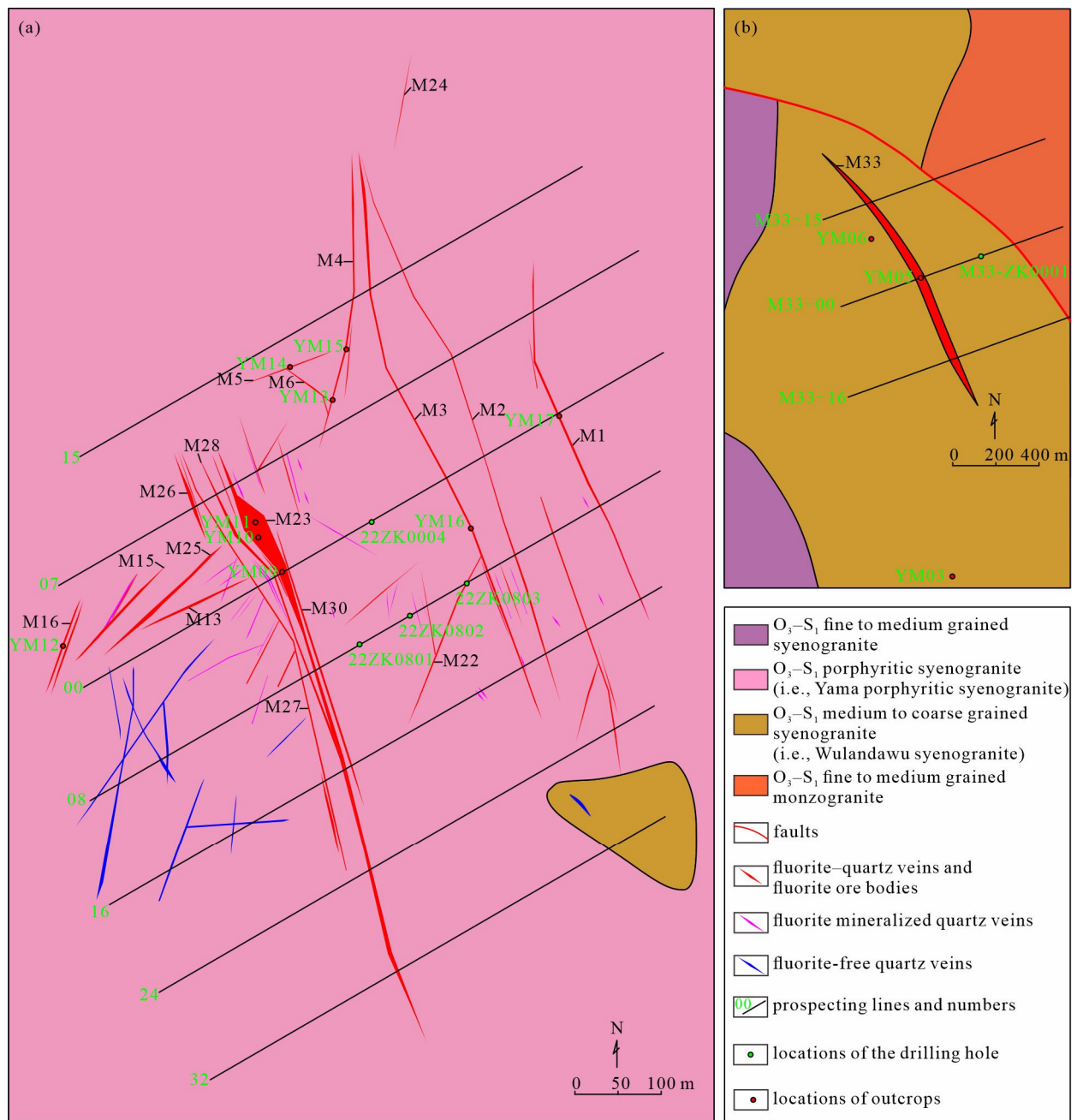


**Figure 4.** Geological map of the Yama fluorite deposit (simplified after [24]). (a) The Yama ore district and (b) the Wulandawu district.

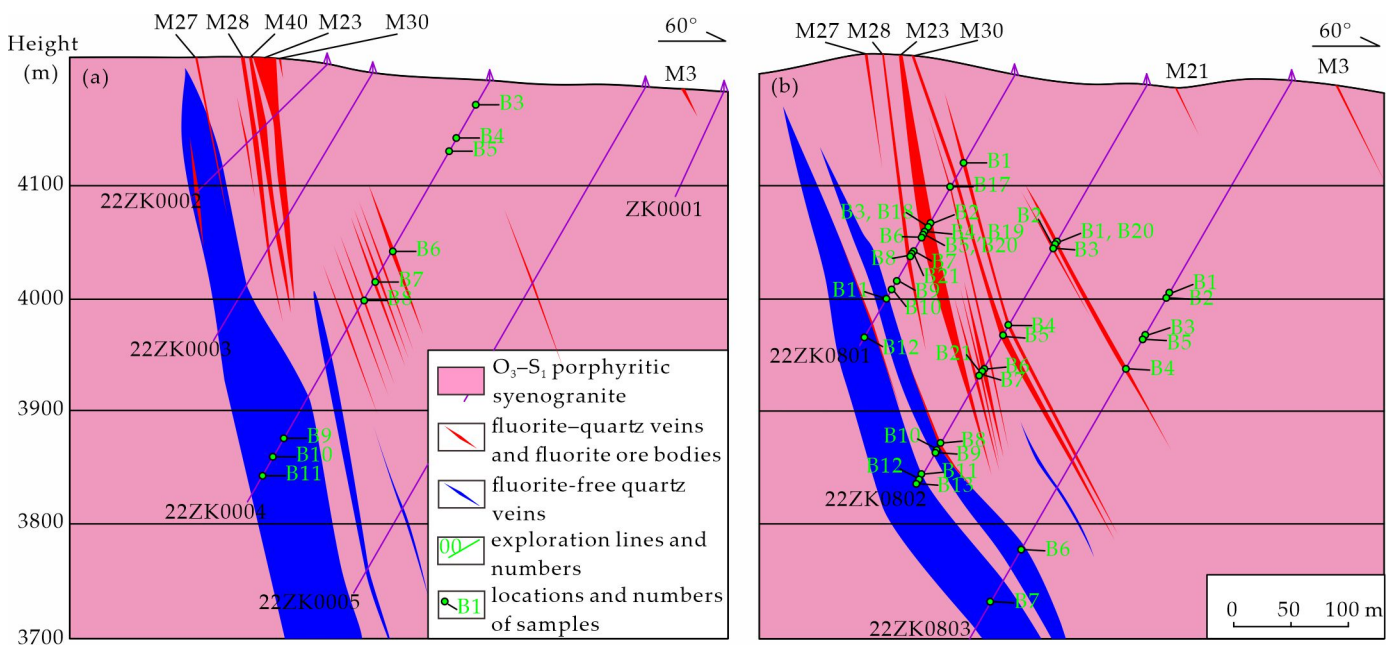


Figure 5. Typical sections of the Yama fluorite deposit (simplified after [24]). (a) Prospecting line 00 and (b) prospecting line 08.

stages minerals	Pre-ore quartz stage	hydrothermal stage	
		fluorite–quartz epoch	quartz–calcite epoch
quartz			
sericite			
fluorite			
calcite			

Figure 6. Paragenetic sequences of minerals in different ore-forming stages in the Yama fluorite deposit. The width of the blue line means the relative mineral abundance, and the length of the blue line means the relative forming period.





**Figure 7.** Photographs and photomicrographs showing the morphology and textural features of the fluorite ores in the Yama fluorite deposit. (a) Photograph and (b,c) photomicrograph of sample 22ZK0801-B20 of Type 1 ore; (d) photograph and (e,f) photomicrograph of sample YM13-B1-B6 of



Type 1 ore; (g) photograph and (h,i) photomicrograph of sample 22ZK0004-B5 of Type 1 ore; (j) photograph and (k,l) photomicrograph of sample YM11-B1-B8 of Type 2 ore; (m) photograph of sample YM09-B5 of Type 2 ore; (n) photograph and (o) photomicrograph of sample 22ZK0803-B5 of Type 2 ore. Qz, quartz; Fl, fluorite; Ser, sericite; Gr, syenogranite; (−), plane-polarized light; (+), cross-polarized light.

### 3. Sampling and Analytical Methods

#### 3.1. Sampling

Seven samples from two types of typical fluorite–quartz veins were collected from drilling holes (22ZK0802, 22ZK0803, and 22ZK0004) in the Yama area (Figures 4a and 5). The other eleven fluorite–quartz vein samples were collected from outcrops (locations YM05, YM09–YM11, YM13, and YM15) in the Yama fluorite deposit (Figure 4a). Table 1 provides detailed descriptions of the samples. In the processing of the selected samples, crushing, conventional magnetic, and heavy liquid separation methods were used to extract quartz for H and O isotopes, fluorites for H, O, and Sr isotopes, as well as for trace element analyses.

**Table 1.** Sample list in the Yama fluorite deposit.

No.	Sample Name	Rock Type	Ore Type	Mineral Assembly	Location
1	22ZK0801-B2	fluorite–quartz vein	Type 1	quartz, fluorite	90.5 m at the core of drilling hole 22ZK0801
2	22ZK0801-B6	breccia-bearing fluorite–quartz vein	Type 2	quartz, fluorite, syenogranite breccia	161.7 m at the core of drilling hole 22ZK0801
3	22ZK0801-B17	fluorite–quartz vein	Type 1	quartz, fluorite	149.4 m at the core of drilling hole 22ZK0801
4	22ZK0802-B21	fluorite–quartz vein	Type 1	quartz, fluorite	253.6 m at the core of drilling hole 22ZK0802
5	22ZK0803-B1	breccia-bearing fluorite–quartz vein	Type 2	quartz, fluorite, syenogranite breccia	202.8 m at the core of drilling hole 22ZK0803
6	22ZK0803-B3	pectinal fluorite–quartz vein	Type 1	quartz, fluorite, minor syenogranite breccia	251.0 m at the core of drilling hole 22ZK0803
7	22ZK0004-B6	pectinal fluorite–quartz vein	Type 2	quartz, fluorite	171.6 m at the core of drilling hole 22ZK0004
8	YM05-B3	fluorite–quartz vein	Type 1	quartz, fluorite, minor sericite	96°01'03" E 37°58'50" N
9	YM05-B7	fluorite–quartz vein	Type 1	quartz, fluorite, minor sericite	96°01'03" E 37°58'50" N
10	YM09-B2	breccia-bearing banded fluorite–quartz vein	Type 2	quartz, fluorite	96°03'58" E 37°57'27" N
11	YM09-B6	breccia-bearing banded fluorite–quartz vein	Type 2	quartz, fluorite, minor sericite	96°03'58" E 37°57'27" N
12	YM10-B2	fluorite–quartz vein	Type 2	quartz, fluorite	96°03'57" E 37°57'31" N
13	YM11-B1	breccia-bearing fluorite–quartz vein	Type 2	quartz, fluorite, syenogranite breccia	96°03'57" E 37°57'31" N
14	YM11-B2	breccia-bearing crusty fluorite–quartz vein	Type 2	quartz, fluorite, minor sericite, syenogranite breccia	96°03'57" E 37°57'31" N
15	YM11-B4	breccia-bearing crusty fluorite–quartz vein	Type 2	quartz, fluorite, minor sericite, syenogranite breccia	96°03'57" E 37°57'31" N

Table 1. Cont.

No.	Sample Name	Rock Type	Ore Type	Mineral Assembly	Location
16	YM11-B6	breccia-bearing crusty fluorite–quartz vein	Type 2	quartz, fluorite, minor sericite, syenogranite breccia	96°03'57" E 37°57'31" N
17	YM13-B2	pectinal fluorite–quartz vein	Type 1	quartz, fluorite, minor sericite	96°04'00" E 37°57'40" N
18	YM15-B1	pectinal fluorite–quartz vein	Type 1	quartz, fluorite	96°04'02" E 37°57'43" N
19	22ZK0802-B16	Yama porphyritic syenogranite	wall rock	alkali feldspar (perthite),	58.6 m at the core of drilling hole 22ZK0802
20	22ZK0802-B18	Yama porphyritic syenogranite		plagioclase, quartz, muscovite, and	138.0 m at the core of drilling hole 22ZK0802
21	22ZK0803-B8	Yama porphyritic syenogranite		biotite, with a few accessory minerals including zircon and epidote	36.3 m at the core of drilling hole 22ZK0803
22	YM03-B1	Wulandawu syenogranite	wall rock	alkali feldspar (perthite),	96°01'29" E 37°58'03" N
23	YM06-B1	Wulandawu syenogranite		plagioclase, quartz, biotite, and	96°01'04" E 37°58'52" N
24	M33-ZK0001-B1	Wulandawu syenogranite		muscovite, with a few accessory minerals including tourmaline, zircon, and epidote	18.0 m at the core of drilling hole 22ZK0803

To compare the Sr isotope of syenogranite wall rocks, six syenogranite samples were collected from drilling holes (22ZK0802, 22ZK0803, and M33-ZK0001-B1) and outcrops (locations YM03 and YM06) (Figure 4). Sample descriptions for the selected syenogranite wall rocks are listed in Table 1 and for detailed descriptions of the samples we refer to our previously published paper [10].

### 3.2. Trace Element and REE Analyses of Fluorites

Trace element contents (excluding REEs) for samples were determined using inductively coupled plasma–atomic emission spectroscopy (ICP–AES) (Agilent 5110 ICP–AES, Santa Clara, CA, USA) and inductively coupled plasma–mass spectrometry (ICP–MS) (Agilent 7900 ICP–MS, Santa Clara, CA, USA) at ALS Chemex (Guangzhou, China) Co., Ltd. Perchloric, nitric, hydrofluoric, and hydrochloric acids were used to digest a prepared sample. The residue was leached with dilute hydrochloric acid and diluted to volume. After that, ICP–AES and ICP–MS were used to analyze it. REEs for samples were also determined using ICP–MS (Agilent 7900 ICP–MS, Santa Clara, CA, USA) at ALS Chemex (Guangzhou, China) Co., Ltd. A prepared sample was added to lithium borate flux, mixed well, and fused in a furnace at 1025 °C. The resulting melt was then cooled and dissolved in an acidic mixture containing nitric, hydrochloric, and hydrofluoric acids. Finally, this solution was analyzed via ICP–MS. The precision for trace elements was better than 10%, which was controlled by the system settings, and the detailed analytical procedure was also referred to in [6].

### 3.3. H, O Isotope Analyses of Fluorites and Quartz

H and O isotope analyses were carried out at the Analytical Laboratory of the Beijing Research Institute of Uranium Geology, China National Nuclear Corporation (BRIUG). The O isotope analysis of quartz was carried out with the bromine pentafluoride method [42]. Water was liberated from 5 to 10 mg of quartz by reaction with BrF<sub>5</sub> and converted to CO<sub>2</sub>

on a platinum-coated carbon rod. The  $\delta^{18}\text{O}$  determinations were made with a Thermo Scientific Delta V Advantage mass spectrometer. Because quartz is an O-bearing mineral, the O isotope of fluid inclusions in quartz, i.e., the  $\delta^{18}\text{O}_{\text{H}_2\text{O}}$  values, should be calculated by using the isotopic fractionation equation of O between quartz and water as shown in Equation (1) as follows [43]:

$$1000\ln\alpha = 3.38 \times 10^6 / T^2 - 3.4 \quad (1)$$

$1000\ln\alpha$  is commonly equal to the value of  $\delta^{18}\text{O}_{\text{quartz}}$  minus  $\delta^{18}\text{O}_{\text{H}_2\text{O}}$ .

By mechanically crushing 5–10 mg of quartz, the H isotopic ratios of decrepitated quartz-hosted fluid inclusions were measured. Samples were heated to 1400 °C in order to release water from fluid inclusions after being degassed for 4 h under vacuum at 105 °C. After that, the released water was captured, reduced to  $\text{H}_2$  by glassy carbon, and then analyzed for  $\delta\text{D}$  values using a Thermo Scientific MAT-253 mass spectrometer.

Through the mechanical crushing of 0.5 g of fluorites, H and O isotopic ratios of decrepitated fluorite-hosted fluid inclusions were measured. Water in fluid inclusions within fluorite samples was first released by heating at 550 °C; then, the released water was trapped, reduced to  $\text{H}_2$  by glassy carbon at 1400 °C, and then analyzed for  $\delta\text{D}$  values using a Thermo Scientific MAT-253 mass spectrometer. Water was liberated from fluorites by reaction with  $\text{BrF}_5$  and converted to  $\text{CO}_2$  on a platinum-coated carbon rod. The  $\delta^{18}\text{O}$  determinations were performed on a Thermo Scientific MAT-253 mass spectrometer.

The results are reported relative to the Vienna Standard Mean Ocean Water (V-SMOW), and the analytical precisions are  $\pm 0.1\text{‰}$  for  $\delta^{18}\text{O}$  and  $\pm 1\text{‰}$  for  $\delta\text{D}$ . The detailed analytical procedures were described in [44].

### 3.4. Sr Isotope Analyses of Fluorites

At Beijing Createch Testing Technology Co., Ltd., (Beijing, China) Sr isotope analyses were performed. Every chemical preparation was carried out on Class 100 work benches within a Class 1000 clean laboratory. A 15 mL Saville™ PFA screw-top beaker was filled with about 150 mg of sample powder. After adding concentrated  $\text{HNO}_3$  and HF (1 mL and 2 mL, respectively) to the samples, the sealed beakers were heated for one week at 150 °C on a hotplate. Following digestion, acids were evaporated on the hotplate and residues were dissolved in 1 mL of concentrated HCl. After that, the same procedures were repeated 3 times. Finally, the samples were dissolved in 1.5 mL of 3.5 M  $\text{HNO}_3$  for Sr purification. Sr-Spec (Triskem, 100–150  $\mu\text{m}$ ) resin was used to separate and purify Sr from samples. Isotopic compositions of Sr analyses were carried out using a Thermo Fisher Scientific Neptune Plus MC-ICP-MS.  $^{87}\text{Sr}/^{86}\text{Sr}$  ratios were corrected for instrumental mass fractionation using the exponential fractionation law and assuming  $^{88}\text{Sr}/^{86}\text{Sr} = 8.375209$ . The analytical methods were modified from those in [45].

Fifteen fluorite and six syenogranite samples were analyzed for Sr isotopic compositions; furthermore, the Sr isotope international standard NBS 987 was repeatedly tested for accuracy monitoring, yielding an average  $^{87}\text{Sr}/^{86}\text{Sr}$  ratio of  $0.710249 \pm 14$  (2SD,  $n = 21$ ) during the analytical procedure of fluorites and  $^{87}\text{Sr}/^{86}\text{Sr}$  ratios =  $0.710247 \pm 13$  (2SD,  $n = 24$ ) during the analytical procedure of syenogranites. Initial  $^{87}\text{Sr}/^{86}\text{Sr}$  ratios (i.e.,  $(^{87}\text{Sr}/^{86}\text{Sr})_i$ ) were calculated based on rock-forming ages for syenogranite wall rocks dated by [10], and on the possible ore-forming ages of fluorites.

## 4. Results

### 4.1. Trace Elements and REEs of Fluorites

The trace element and REE data for fluorites are listed in Table 2. Most trace and REE elements show concentrations of <10 ppm. Relatively high concentrations (a few to several tens of ppm) were observed for Rb (1.8–21.5 ppm), Sr (15.2–64.5 ppm), Y (2.2–107 ppm), and Ba (1.8–13.3 ppm), whereas very low concentrations (usually <1 ppm) were found for Fe, Co, W, Pb, Th, U and some of REEs, such as Eu, Tb, Tm, and Lu, and some of them were even below the detection limits, such as Mg, Mn, Ni, Zn, Nb, Cd, Mo, Sn, Sb, Hf, and Ta.

**Table 2.** Trace elements and REEs of fluorites in the Yama fluorite deposit.

Sample Name	22ZK0801-B2	22ZK0802-B21	22ZK0803-B3	YM05-B3	YM05-B7	22ZK0004-B6	YM09-B2	YM09-B6	YM10-B2	YM11-B2	YM11-B4	YM11-B6	YM13-B2	YM15-B1
Types	Type 1	Type 1	Type 1	Type 1	Type 1	Type 2	Type 2	Type 2	Type 2	Type 2	Type 2	Type 2	Type 1	Type 1
Li	2.60	3.60	1.90	5.20	5.20	2.80	0.50	2.30	7.00	0.60	0.70	0.60	1.80	1.70
Be	0.1	0.4	0.1	0.4	0.5	0.2	0.8	0.6	7.5	<0.05	<0.05	0.1	0.21	0.13
Mg	<0.01	0.01	0.01	0.01	0.01	<0.01	<0.01	0.01	0.01	<0.01	<0.01	<0.01	0.02	0.01
Sc	0.1	0.1	0.1	0.1	0.1	0.1	0.1	0.1	0.1	0.1	0.1	0.1	0.1	0.1
Ti	<0.005	<0.005	<0.005	<0.005	<0.005	<0.005	<0.005	<0.005	<0.005	<0.005	<0.005	<0.005	<0.005	<0.005
V	1	1	1	1	2	1	1	1	1	<1	1	<1	1	1
Cr	1	1	1	1	1	<1	<1	<1	1	1	<1	1	<1	<1
Mn	<5	<5	<5	<5	<5	<5	<5	<5	<5	<5	<5	<5	<5	<5
Fe	0.01	0.01	0.01	0.04	0.04	0.01	0.01	<0.01	0.01	0.01	<0.01	0.01	0.02	0.01
Co	0.7	0.6	0.7	0.6	0.7	0.7	0.7	0.7	0.6	0.8	0.8	0.8	0.8	0.8
Ni	<0.2	<0.2	<0.2	<0.2	<0.2	<0.2	<0.2	<0.2	<0.2	<0.2	<0.2	<0.2	<0.2	<0.2
Cu	0.8	0.5	0.6	0.6	1.2	0.8	0.8	0.8	0.6	0.8	0.6	0.8	0.8	0.5
Zn	<2	<2	<2	<2	<2	<2	<2	<2	<2	<2	<2	<2	<2	<2
Ga	0.2	0.3	0.2	1.3	1.6	0.2	0.3	0.2	0.5	0.2	0.1	0.2	0.25	0.23
Rb	2.6	4.6	4.4	20.0	21.5	5.3	3.5	2.8	6.9	2.3	1.8	3.3	4.1	3
Sr	20.1	18.3	17.8	64.5	54.3	21.2	15.2	15.2	17	23.1	22.2	22	21.9	26.7
Y	11.2	14.0	29.5	107.0	64.1	5.6	7.5	3.2	8.2	2.9	2.2	2.7	53.9	5.9
Zr	3.00	<2	<2	3.00	<2	<2	3.00	4.00	6.00	3.00	<2	<2	<2	3
Nb	<0.1	<0.1	<0.1	0.10	0.10	<0.1	0.10	0.10	<0.1	0.10	<0.1	<0.1	<0.1	<0.1
Mo	<0.05	<0.05	0.09	0.06	<0.05	<0.05	<0.05	0.05	0.42	<0.05	<0.05	<0.05	0.07	0.42
Cd	<0.02	<0.02	<0.02	<0.02	<0.02	<0.02	<0.02	<0.02	<0.02	<0.02	<0.02	<0.02	<0.02	<0.02
Sn	<0.2	<0.2	<0.2	<0.2	<0.2	<0.2	<0.2	<0.2	<0.2	<0.2	<0.2	<0.2	<0.2	0.2
Sb	<0.05	<0.05	<0.05	0.07	0.06	<0.05	0.3	<0.05	0.08	<0.05	<0.05	<0.05	<0.05	<0.05
Cs	0.2	0.3	0.2	1.0	1.1	0.2	0.1	0.1	0.3	0.1	0.1	0.1	0.2	0.21
Ba	2.3	7.0	2.1	2.1	2.4	5.6	2.6	3.5	1.8	4.3	13.3	8.1	6.9	6.3
Ca	47.00	46.70	>50	46.20	46.70	>50	49.10	48.50	45.50	>50	>50	>50	>50	49.8
La	0.8	1.4	7.6	1.4	1.1	0.4	0.6	0.3	0.2	1.2	0.3	0.4	1.2	1.2
Ce	1.60	2.70	16.20	3.10	2.40	0.90	1.00	0.40	0.20	2.00	1.30	1.20	3	1.7
Pr	0.18	0.30	1.86	0.51	0.39	0.10	0.15	0.06	0.03	0.19	0.06	0.09	0.37	0.3
Nd	0.80	1.20	6.80	2.30	1.80	0.40	0.60	0.20	0.20	0.70	0.20	0.30	1.5	1.1
Sm	0.32	0.32	1.77	1.21	0.93	0.13	0.19	0.08	0.08	0.10	0.09	0.10	0.66	0.25
Eu	0.03	0.05	0.14	0.10	0.08	<0.02	0.02	<0.02	<0.02	0.02	<0.02	<0.02	0.09	0.04
Gd	0.63	0.62	2.30	3.10	2.07	0.24	0.35	0.15	0.23	0.23	0.15	0.17	1.65	0.41
Tb	0.13	0.13	0.42	0.71	0.49	0.06	0.08	0.03	0.05	0.05	0.03	0.04	0.37	0.07
Dy	1.02	1.04	2.91	5.88	3.96	0.44	0.63	0.24	0.44	0.31	0.24	0.29	3.39	0.5
Ho	0.24	0.26	0.66	1.45	1.00	0.11	0.15	0.06	0.14	0.07	0.05	0.06	0.94	0.12
Er	0.77	0.90	2.12	4.33	3.00	0.32	0.47	0.19	0.47	0.19	0.16	0.19	3.54	0.34

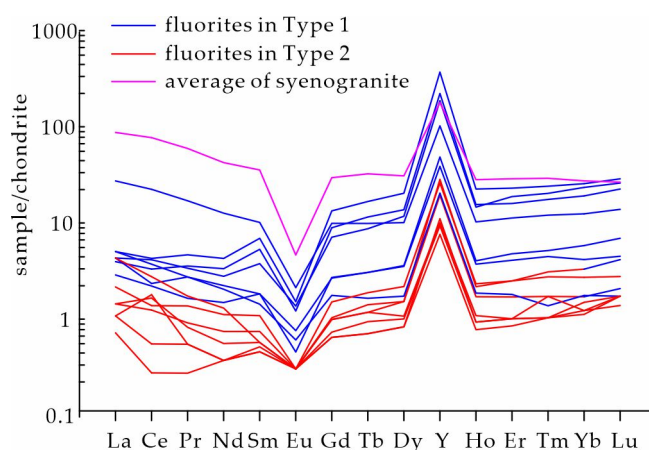


Table 2. Cont.

Sample Name	22ZK0801-B2	22ZK0802-B21	22ZK0803-B3	YM05-B3	YM05-B7	22ZK0004-B6	YM09-B2	YM09-B6	YM10-B2	YM11-B2	YM11-B4	YM11-B6	YM13-B2	YM15-B1
Tm	0.1	0.2	0.4	0.7	0.5	0.1	0.1	0.0	0.1	0.0	0.0	0.1	0.59	0.04
Yb	0.78	1.09	2.33	4.80	3.58	0.32	0.51	0.28	0.62	0.21	0.23	0.23	4.39	0.33
Lu	0.1	0.2	0.4	0.8	0.7	0.1	0.1	0.1	0.1	0.1	0.1	0.0	0.75	0.05
Hf	0.1	<0.1	<0.1	<0.1	<0.1	<0.1	<0.1	<0.1	<0.1	<0.1	<0.1	<0.1	<0.1	<0.1
Ta	<0.05	<0.05	<0.05	<0.05	<0.05	<0.05	<0.05	<0.05	<0.05	<0.05	<0.05	<0.05	<0.05	<0.05
W	0.1	0.2	0.1	0.2	0.4	0.1	0.1	0.1	0.1	<0.1	<0.1	<0.1	0.3	0.1
Pb	1.00	<0.5	<0.5	0.70	0.70	<0.5	<0.5	1.30	6.00	<0.5	0.60	<0.5	26.3	<0.5
Bi	2.35	0.02	0.10	0.25	0.11	0.74	0.05	8.31	15.15	2.64	1.87	1.55	0.16	0.01
Th	0.31	0.16	0.34	0.54	0.30	0.21	0.43	0.27	<0.05	0.11	0.06	0.08	2.77	1.13
U	0.15	0.21	1.04	0.47	0.63	0.23	0.14	0.21	0.29	0.28	0.19	0.19	0.30	0.28
∑REEs	7.56	10.36	45.86	30.42	21.96	3.53	4.91	2.07	2.87	5.35	2.89	3.16	22.44	6.45
LREEs/HREEs	0.97	1.36	2.99	0.40	0.44		1.09			3.69			0.44	2.47
(La/Yb) <sub>N</sub>	0.69	3.34	1.89	8.43	4.24	1.29	3.03	0.77	1.02	0.75	0.85	1.03	7.62	1.20
(La/Sm) <sub>N</sub>	0.82	0.60	0.79	0.77	0.70	0.86	0.78	0.54	0.45	0.93	0.66	0.79	0.49	0.95
Eu/Eu*	0.20	0.34	0.21	0.16	0.18		0.24			0.40			0.26	0.38
Y/Y*	1.64	1.95	1.54	2.65	2.33	1.84	1.77	1.93	2.39	1.43	1.45	1.48	2.19	1.74

Note: Units for Ca, Mg, Fe, and Ti are wt. %, and units for other trace elements are ppm. ∑REEs—total REE contents, LREEs—light rare earth elements, including La, Ce, Pr, Nd, Sm, and Eu, HREEs—heavy rare earth elements, including Gd, Tb, Dy, Ho, Er, Tm, Yb, and Lu, Eu/Eu\* =  $Eu_N / \sqrt{[Sm_N \times Gd_N]}$ , Y/Y\* =  $(Y_N) / \sqrt{[Dy_N \times Ho_N]}$ . REE normalization values were obtained from [46]. The Y normalization value was obtained from [47].

The total REE contents ( $\Sigma$ REEs) in studied fluorites are relatively low (<2.09–45.86 ppm), i.e., 2.89–30.42 ppm for the fluorites in Type 1 ores, and 2.09–45.89 ppm for the fluorites in Type 2 ores. The Y concentrations for all types of fluorites are relatively high, i.e., 5.90–107 ppm for the fluorites in Type 1 ores and 2.20–29.50 ppm for the fluorites in Type 2 ores. In general, Type 1 ores have slightly higher total REE contents and Y contents than Type 2 ores (Table 2). In chondrite-normalized REE, including Y, pattern (namely a REY pattern) diagrams (Y inserted between Dy and Ho), the fluorite samples have roughly similar chondrite-normalized REY patterns, basically indicating a similar source and ore genesis. They are also characterized by relatively strong enrichment in heavy rare earth elements (HREEs), showing negative Eu anomalies ( $\text{Eu}/\text{Eu}^* = 0.16\text{--}0.40$ , Table 2), strongly positive Y anomalies ( $\text{Y}/\text{Y}^* = 1.43\text{--}2.39$ , Table 2), and relatively high  $(\text{La}/\text{Yb})_N$  values of 0.69–8.43 (Figure 8), although fluorites in Type 1 ores show higher total REE contents (average = 14.58 ppm) than those in Type 2 ores (average = 9.69 ppm). However, both types of fluorite ores show slightly different chondrite-normalized REY patterns compared to the average of syenogranite wall rocks (which show a flat HREE pattern and are slightly enriched in LREEs) relative to HREEs as described in our previously published paper [10].



**Figure 8.** Chondrite-normalized REE and Y element patterns of fluorites in the Yama fluorite deposit. REE normalization values were obtained from [46]. The Y normalization value was obtained from [47].

#### 4.2. H and O Isotopic Compositions of Quartz

The Yama fluorite deposit contains fluorites with varying  $\delta\text{D}$  and  $\delta^{18}\text{O}$  values from  $-77.4\text{‰}$  to  $-102.4\text{‰}$  (average =  $-90.1\text{‰}$ ) and from  $-12.7\text{‰}$  to  $-4.3\text{‰}$  (average =  $-8.0\text{‰}$ ), respectively (Table 3). These values indicate the initial isotope compositions of the ore-forming fluids in the Yama fluorite deposit. The  $\delta\text{D}$  value ranges of two types of fluorite ores overlap each other, but Type 2 samples have slightly heavier  $\delta^{18}\text{O}$  values than Type 1 (Figure 9).

**Table 3.** H and O isotope data for quartz and fluorites in the Yama fluorite deposit.

No.	Sample Name	Rock Type	Mineral	$\delta\text{D}_{\text{V-SMOW}}$ (‰)	$\delta^{18}\text{O}_{\text{V-SMOW}}$ (‰)	$\delta^{18}\text{O}_{\text{H}_2\text{O}}$ (‰) *
1	22ZK0801-B2	Type 1	quartz	−82.1	−3.6	−17.2
2	22ZK0801-B17	Type 1	quartz	−85.3	−2.8	−16.4
3	22ZK0802-B21	Type 1	quartz	−80.6	−3.6	−17.2
4	22ZK0803-B3	Type 1	quartz	−87.3	−4.2	−17.8
5	22ZK0004-B6	Type 2	quartz	−83.6	−1.4	−15.0
6	YM09-B2	Type 2	quartz	−86.0	−3.4	−17.0
7	YM10-B2	Type 2	quartz	−83.6	−2.7	−16.3
8	YM11-B1	Type 2	quartz	−91.2	−4.5	−18.1
9	YM11-B4	Type 2	quartz	−86.1	−4.2	−17.8
10	YM11-B6	Type 2	quartz	−82.9	−4.4	−18.0

Table 3. Cont.

No.	Sample Name	Rock Type	Mineral	$\delta D_{V-SMOW}$ (‰)	$\delta^{18}O_{V-SMOW}$ (‰)	$\delta^{18}O_{H_2O}$ (‰) *
11	YM13-B2	Type 1	quartz	−81.0	−2.3	−15.9
12	YM15-B1	Type 1	quartz	−79.6	−2.6	−16.2
13	22ZK0801-B2	Type 1	fluorite	−84.7	−12.7	
14	22ZK0801-B6	Type 2	fluorite	−88.8	−9.1	
15	22ZK0802-B21	Type 1	fluorite	−89.3	−10.2	
16	22ZK0803-B1	Type 2	fluorite	−92.1	−11.7	
17	22ZK0803-B3	Type 1	fluorite	−87.0	−9.8	
18	YM05-B3	Type 1	fluorite	−77.4	−9.1	
19	22ZK0004-B6	Type 2	fluorite	−83.3	−10.7	
20	YM09-B2	Type 2	fluorite	−83.5	−4.6	
21	YM09-B6	Type 2	fluorite	−92.6	−4.4	
22	YM10-B2	Type 2	fluorite	−97.1	−4.3	
23	YM11-B2	Type 2	fluorite	−98.2	−5.0	
24	YM11-B4	Type 2	fluorite	−94.6	−5.7	
25	YM11-B6	Type 2	fluorite </tr			

\* The calculated  $\delta^{18}O_{H_2O}$  values of the fluids are based on an average homogenization temperature of quartz of 173 °C using Equation (1) [43].

The Yama fluorite deposit contains quartz in different types of fluorite ores with slightly invariable  $\delta D$  values ranging from  $-91.2\text{‰}$  to  $-79.6\text{‰}$  (average =  $-84.1\text{‰}$ ). The values are within the range of  $\delta D$  values of fluorite (Figure 9). The quartz in different types of fluorite ores in this deposit also has invariable  $\delta^{18}O$  values ranging from  $-4.5\text{‰}$  to  $-1.4\text{‰}$  (average =  $-3.3\text{‰}$ ). Calculating the precise  $\delta^{18}O_{H_2O}$  values of fluids that were in equilibrium with the quartz is challenging due to the large variation in temperatures obtained from fluid inclusions (e.g., [48]). However, for a temperature range of 200–500 °C, Equation (1) provides a good approximation of the isotopic fractionation of O between quartz and water [43]. However, the homogenization temperatures of quartz in fluorite–quartz veins ranged from 135 °C to 209 °C (average = 173 °C) in the Yama fluorite deposit (unpublished data). Therefore, if using 173 °C as the trapping temperature, the calculated  $\delta^{18}O_{H_2O}$  values of the fluids for fluid inclusions from the quartz in fluorite ores were from  $-18.0\text{‰}$  to  $-15.0\text{‰}$  (Table 3), which are totally different from the analytical O isotopic data from  $-12.7\text{‰}$  to  $-4.3\text{‰}$  of fluorite (Figure 9).

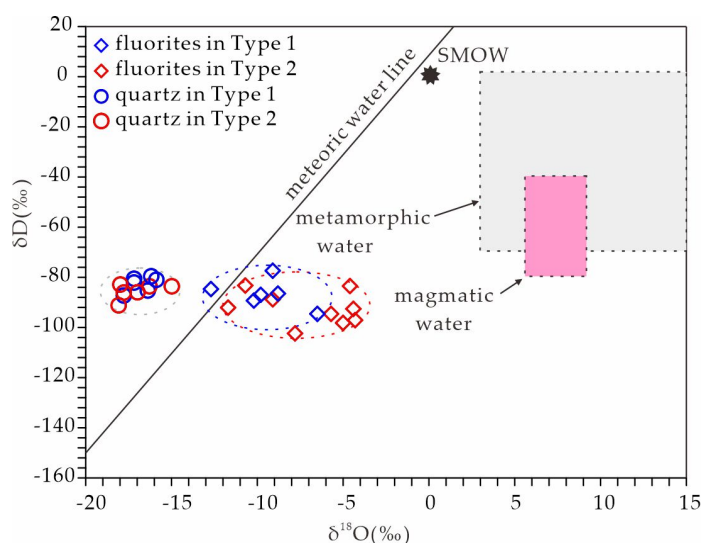


Figure 9. Plot of  $\delta D$  versus  $\delta^{18}O$  diagram in the Yama fluorite deposit. Magmatic and metamorphic water fields after [49].

#### 4.3. Sr Isotopic Compositions of Fluorites

Table 4 lists the Sr isotopic compositions of fluorites. The samples for the Yama porphyritic syenogranite and the Wulandawu syenogranite have variable analytical  $^{87}\text{Sr}/^{86}\text{Sr}$  ratios of 0.832625–0.880566 and 1.056637–1.191950, respectively. Based on the average age of their rock-forming ages of 444.3 Ma and 441.2 Ma [10], their calculated initial  $^{87}\text{Sr}/^{86}\text{Sr}$  ratios (i.e.,  $(^{87}\text{Sr}/^{86}\text{Sr})_i$ ) are 0.660469–0.678689 and 0.668841–0.697535, respectively.

**Table 4.** Sr isotopic compositions of fluorites and syenogranites from the Yama fluorite deposit.

Sample Name	Rock/Mineral Types	Rb <sup>a</sup> (ppm)	Sr <sup>a</sup> (ppm)	$^{87}\text{Rb}/^{86}\text{Sr}$	$^{87}\text{Sr}/^{86}\text{Sr}$	$\pm 2\sigma$	$(^{87}\text{Sr}/^{86}\text{Sr})_i$ <sup>b</sup>	$(^{87}\text{Sr}/^{86}\text{Sr})_i$ <sup>c</sup>
22ZK0801-B2	Type 1	2.6	20.1	0.374295	0.753393	0.000007	0.751031	
22ZK0801-B6	Type 2	2.6	20.1	0.374295	0.753517	0.000008	0.751155	
22ZK0802-B21	Type 1	4.6	18.3	0.727351	0.755463	0.000008	0.750873	
22ZK0803-B1	Type 2	4.4	17.8	0.715269	0.754075	0.000007	0.749562	
22ZK0803-B3	Type 1	4.4	17.8	0.715269	0.755551	0.000007	0.751037	
YM05-B3	Type 1	20	64.5	0.897237	0.828185	0.000008	0.822523	
22ZK0004-B6	Type 2	5.3	21.2	0.723398	0.756299	0.000006	0.751734	
YM09-B2	Type 2	3.5	15.2	0.666287	0.756628	0.000006	0.752424	
YM09-B6	Type 1	2.8	15.2	0.533030	0.753935	0.000009	0.750571	
YM10-B2	Type 2	6.9	17	1.174457	0.754550	0.000007	0.747139	
YM11-B2	Type 2	2.3	23.1	0.288106	0.752564	0.000006	0.750746	
YM11-B4	Type 2	1.8	22.2	0.234615	0.751325	0.000008	0.749845	
YM11-B6	Type 2	3.3	22	0.434039	0.753245	0.000006	0.750506	
YM13-B2	Type 1	4.1	21.9	0.541722	0.749089	0.000007	0.745671	
YM15-B1	Type 1	3	26.7	0.325122	0.753748	0.000006	0.751696	
22ZK0802-B16	Yama syenogranite	374	37.6	28.781987	0.854448	0.000009		0.672287
22ZK0802-B18	Yama syenogranite	439	46.7	27.200986	0.832625	0.000008		0.660469
22ZK0803-B8	Yama syenogranite	377	34.2	31.897178	0.880566	0.000007		0.678689
YM03-B1	Wulandawu syenogranite	477	20.5	67.328902	1.091983	0.000010		0.668841
YM06-B1	Wulandawu syenogranite	443	23.7	54.086938	1.056637	0.000009		0.716716
M33-ZK0001-B1	Wulandawu syenogranite	522	19.2	78.669482	1.191950	0.000013		0.697535

<sup>a</sup> Contents determined by ICP-MS (fluorites from Table 2, and syenogranites from [10]). <sup>b</sup> Recalculation of  $(^{87}\text{Sr}/^{86}\text{Sr})_i$  ratios to 443 Ma for fluorites (ages obtained from [10]). <sup>c</sup> Recalculation of  $(^{87}\text{Sr}/^{86}\text{Sr})_i$  ratios to 444.3 Ma for the Yama porphyritic syenogranite, and to 441.2 Ma for the Wulandawu syenogranite (ages obtained from [10]), using  $\lambda^{87}\text{Rb} = 1.42 \times 10^{-11} \text{ year}^{-1}$  [50].

Both types of fluorites have variable  $^{87}\text{Sr}/^{86}\text{Sr}$  ratios ranging from 0.749089 to 0.828185, with an average of 0.758771. However, except for an anomalously high ratio of 0.828185 for the sample YM05-B3, the other analytical  $^{87}\text{Sr}/^{86}\text{Sr}$  ratios are focused on a relatively invariable range of 0.749089–0.756628, with an average of 0.753813. As we do not know the exact ore-forming age of fluorite ore bodies in the Yama fluorite deposit, it should be considered to be either the same or later than the rock-forming ages of the syenogranite wall rocks, as provided by [10]. If the ore-forming age is equal to the average formation age of 443 Ma of syenogranite wall rocks provided in [10], the initial  $^{87}\text{Sr}/^{86}\text{Sr}$  ratios for fluorites can be calculated as ranging from 0.745671 to 0.822523, with an average of 0.755101 (Figure 10). If we discarded the anomalously high ratio of 0.822523 for the sample YM05-B3, the calculated  $(^{87}\text{Sr}/^{86}\text{Sr})_i$  ratios of 0.745671 to 0.751696 for fluorites in Type 1 ores are very similar to the calculated  $(^{87}\text{Sr}/^{86}\text{Sr})_i$  ratios of 0.747139 to 0.752424 for fluorites in Type 2 ores, and both  $(^{87}\text{Sr}/^{86}\text{Sr})_i$  ratios of fluorites are relatively invariable, ranging from 0.745671 to 0.752424.



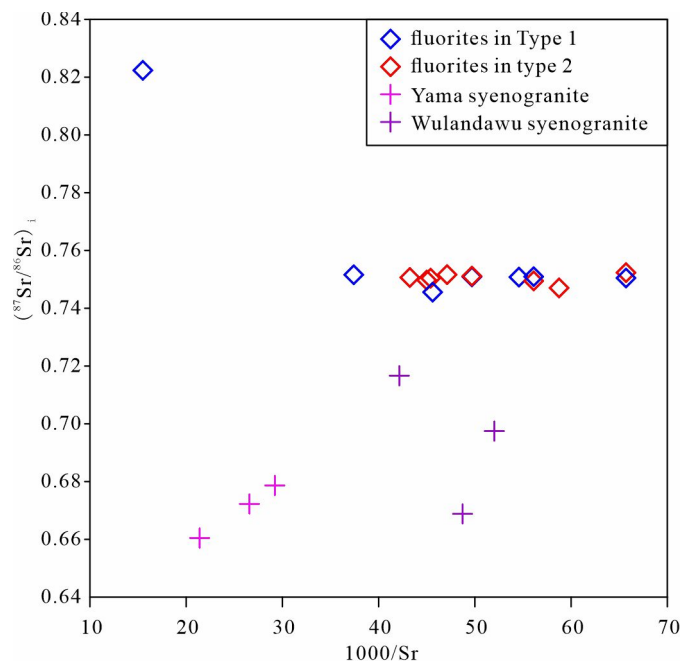


**Figure 10.** Plot of calculated ( $^{87}\text{Sr}/^{86}\text{Sr}$ )<sub>i</sub> ratio versus 1000/Sr for fluorites and syenogranite wall rocks from the Yama fluorite deposit. All isotopic data for fluorites are corrected at the average rock-forming age (443 Ma) of syenogranite wall rocks [10]. All isotopic data for syenogranites are corrected at their own rock-forming age, i.e., 444.3 Ma for the Yama porphyritic syenogranite and 441.2 Ma for the Wulandawu syenogranite [10].

## 5. Discussion

### 5.1. Origin of Ore-Forming Fluids for Fluorite Mineralization

A latitude effect on  $\delta\text{D}$  values has been proposed for fluorite deposits in Eastern China [51]. The  $\delta\text{D}$  value of these deposits decreases with increasing latitude, with implications of a significant origin from meteoric water. Figure 9 shows the hydrogen and oxygen isotopic compositions of fluorites in the Yama fluorite deposit. Both types of fluorites display relatively unvaried  $\delta\text{D}$  values and variable  $\delta^{18}\text{O}_{\text{H}_2\text{O}}$  values, and they roughly overlap with each other. The plot of the data is close to the meteoric water line with relatively lower  $\delta\text{D}$  values than the typical composition of magmatic or metamorphic water, indicating that the ore-forming fluids might predominantly be meteoric water. Their relatively constant  $\delta\text{D}$  values might indicate there is no apparent H isotope exchange between the ore-forming water and wall rocks.

The  $\delta^{18}\text{O}_{\text{H}_2\text{O}}$  values of different types of fluorites have a more variable range; thus, samples show a horizontal trend in  $\delta^{18}\text{O}_{\text{H}_2\text{O}}$  values (“O isotope shift”) extending from the meteoric water line, which might result from possible fluid–rock interactions either before or during fluorite mineralization (e.g., [52]). Certainly, mixing with minor other deep water also cannot be totally precluded. Because quartz–fluorite veins were dominantly filled in the brittle faults within syenogranite wall rocks, rare fluid–rock interactions happened during fluorite mineralization, which is proven by the different initial Sr isotopic compositions between fluorites and syenogranite wall rocks and rare alterations close to fluorite–quartz veins within the syenogranite wall rocks. Therefore, the  $\delta^{18}\text{O}_{\text{H}_2\text{O}}$  values of fluorite samples showing an O isotope shift extending from the meteoric water line may have resulted from possible deep fluid–rock interactions before fluorite mineralization. The fluorites in Type 2 ores have slightly heavier and variable  $\delta^{18}\text{O}_{\text{H}_2\text{O}}$  values than those in Type 1 ores, possibly because they contain some syenogranite breccias within such breccia-bearing fluorite–quartz veins. There would also possibly be a slight exchange between ore-forming fluids and syenogranite breccias during fluorite mineralization.

Compared to fluorites, the quartz in different fluorite ores has a similar  $\delta D$  value range for fluid inclusions to those of fluorites (Figure 9); however, their calculated  $\delta^{18}O_{VSMOW}$  values from  $-18.0\text{‰}$  to  $-15.0\text{‰}$  for fluid inclusions from the quartz in the Yama fluorite deposit are totally different from the analytical  $\delta^{18}O_{H_2O}$  values from  $-12.7\text{‰}$  to  $-4.3\text{‰}$  of different types of fluorites. We have argued that the reasons might be as follows: firstly, the trapping temperature ( $173\text{ °C}$ ) is lower than the temperature range of  $200\text{--}500\text{ °C}$  for Equation (1), which is used as a good approximation of isotopic fractionation of O between quartz and water [43]; secondly, bulk fluids extracted from quartz, which are a mixture of primary, pseudosecondary, and secondary inclusions, usually reflect H and O isotopic compositions of important secondary fluid inclusions formed in the presence of meteoric water during the uplift of the deposits (e.g., [53–55]). Therefore, the H and O isotopic compositions for the ore-forming fluids should be represented by the data obtained from studied fluorites rather than quartz, in particular from those fluorites which usually contain more cleavages than quartz and cannot trap the considerable secondary fluid inclusions. These are consistent with our microscopic observations.

In conclusion, the origin of ore-forming fluids for the Yama fluorite mineralization might predominantly originate from paleo-meteoric water, but a mixture with certain deep-water sources (e.g., magmatic water or metamorphic water) cannot be totally precluded.

### 5.2. Source of Ore-Forming Materials for Fluorite Mineralization

Because strontium and calcium have similar geochemical natures, fluorites are therefore usually characterized by enriched Sr and depleted Nd and could keep their initial Sr isotopic compositions when they are formed. Two types of fluorites typically have invariable analytical  $^{87}Sr/^{86}Sr$  ratios of  $0.749089\text{--}0.756628$  with an average of  $0.753813$ , except for the anomalously high ratio. In addition, the corresponding calculated  $(^{87}Sr/^{86}Sr)_i$  ratios for both types of fluorites, which range from  $0.745671$  to  $0.752424$  with an average of  $0.750285$  based on the average formation age of  $443\text{ Ma}$  of syenogranite wall rocks [10], are apparently higher than the calculated  $(^{87}Sr/^{86}Sr)_i$  ratios of  $0.660469\text{--}0.697535$  of the syenogranite wall rocks (Figure 10). If a younger ore-forming age than the  $443\text{ Ma}$  is used, then the calculated  $(^{87}Sr/^{86}Sr)_i$  ratios should be larger than the range of  $0.745671\text{--}0.752424$  with the corrected age of  $443\text{ Ma}$ . Furthermore, they will be larger than the calculated  $(^{87}Sr/^{86}Sr)_i$  ratios of  $0.660469\text{--}0.697535$  of the syenogranite wall rocks. Therefore, whatever the ore-forming age which was the same or younger than  $443\text{ Ma}$ , the calculated  $(^{87}Sr/^{86}Sr)_i$  ratios of fluorites should be much greater than the calculated  $(^{87}Sr/^{86}Sr)_i$  ratios of the syenogranite wall rocks. This indicates that the Sr source should be predominantly derived from the ore-forming fluids themselves rather than from the syenogranite wall rocks, as do other ore-forming materials. This argument has further been proven by the geological fact that the fluorite–quartz veins were formed by the low-temperature-filling mineralization rather than by an apparent water–rock reaction between the ore-forming fluids and syenogranite wall rocks.

### 5.3. Implication for the Genesis of Fluorite Mineralization

The Tb/Ca ratio can reveal the assimilation of Ca from the surrounding rocks or the adsorption of REEs during the crystallization of fluorite [56]. The Tb/La ratio can be employed to evaluate both the fractionation degree of REEs in fluorite and the reactivation of fluorite [57,58]. Therefore, the Tb/Ca versus Tb/La diagram was used to discriminate fluorite genetic types, i.e., pegmatitic, hydrothermal, and sedimentary genesis [56]. In this study, four fluorites in Type 2 and two samples in Type 1 have a Ca content of  $>50\%$  (the detection limit) by LA-ICP-MS trace element analyses; therefore, it is approximated that  $n(Ca)$  is equal to the theoretical value ( $51.3328\%$ ) in  $CaF_2$  (e.g., [59]). Meanwhile, the Tb/Ca ratios are calculated for such samples. In this way, fluorites in Type 1 ores in the Yama fluorite deposit predominantly plot in the hydrothermal field on the Tb/Ca versus the Tb/La diagram (Figure 11a); meanwhile, fluorites in Type 2 ores predominantly plot in the sedimentary field in the Tb/Ca versus the Tb/La diagram (Figure 11a). Moreover,

as the partitioning behavior of Dy into fluorite is similar to that of Tb [56], Dy can be substituted for Tb in the Tb/Ca versus the Tb/La discrimination diagram [60]. Similarly, in the Dy/Ca vs. Dy/La plot (Figure 11b), fluorites in Type 1 ores also predominantly plot in the hydrothermal field, and fluorites in Type 2 ores predominantly plot in the sedimentary field. Therefore, it is reasonably considered that the crusty structures for fluorite in Type 2 ores might not only indicate the low-temperature structure but also the slow speed of crystallization of ore-forming fluids while they infilled in the ore-controlling faults. The process of such low-temperature and slow-speed crystallization of the ore-forming fluids might be similar to a chemical sedimentary process; therefore, they plot in the sedimentary fields in the Tb/Ca vs. Tb/La plot (Figure 11a) or the Dy/Ca vs. Dy/La plot (Figure 11b). However, with geological observations in the field, fluorite–quartz veins in the study area were all infilled along the faults within the syenogranite wall rocks; thus, indicating that all types of fluorites within fluorite–quartz veins should be a hydrothermal filling genesis. In the Tb/Ca vs. Tb/La plot (Figure 11a), fluorites in the Type 1 ore also show a crystallization trend, indicating normal hydrothermal crystallization. The slightly increased Tb/La atom ratios (Figure 11) and the increased  $\Sigma$ REE contents (Table 2) in fluorites from Type 2 to Type 1 ores suggest that REEs in the ore-forming fluid were gradually fractionated. This is consistent with the fact that fine-grained fluorites showing crusty or colloform structures in Type 2 ores were crystallized earlier than other fluorites within fluorite–quartz veins (Figures 6 and 7), and the more perfect crystal structure of fluorite might be more suitable for the entry of REEs (e.g., [61]).

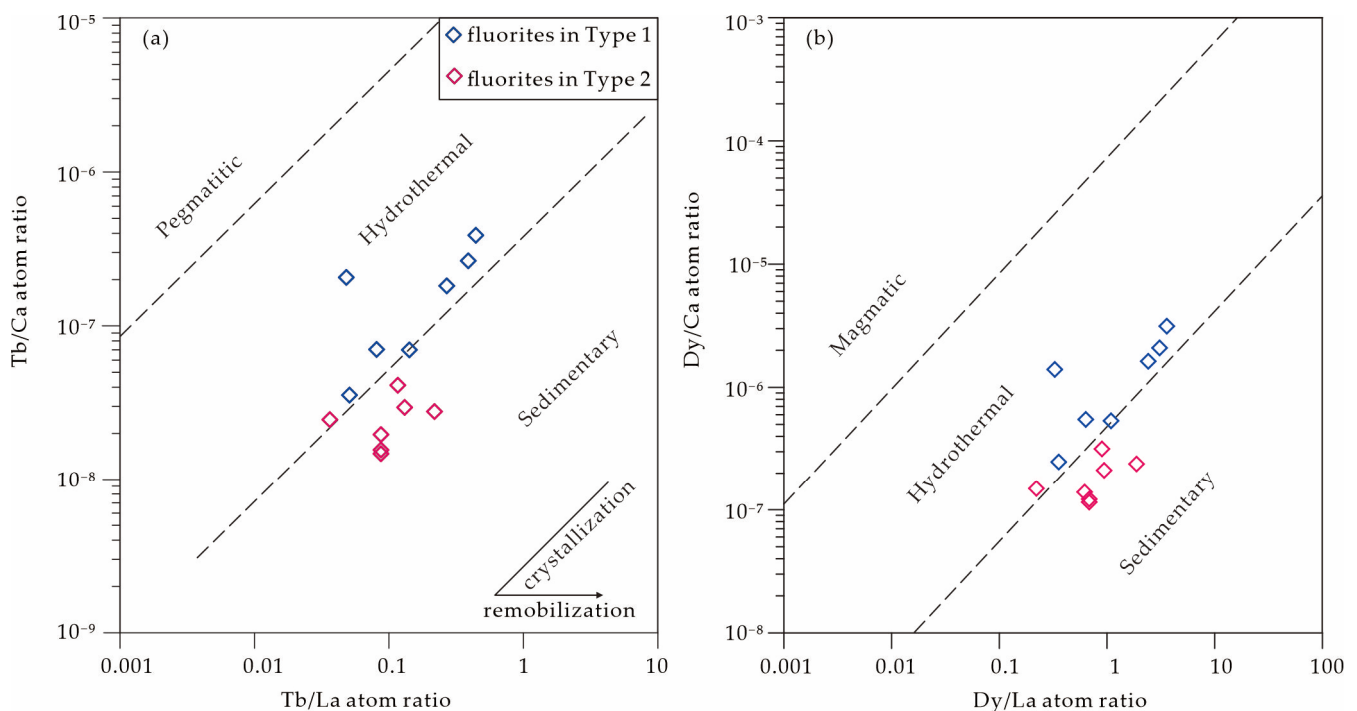


**Figure 11.** (a) Plot of Tb/Ca versus Tb/La ratios for fluorites in the Yama fluorite deposit (the base map was modified from [56]); (b) plot of Dy/Ca versus Dy/La for fluorites in the Yama fluorite deposit (the base map was modified from [60]).

Moreover, the Y/Ho ratios of fluorite can be used to determine the origin of the fluid because the Y and Ho have comparable ionic radii and potentials [58], and the Y/Ho ratios of fluorite from the same origin are usually constant [62]. In this study, the Y contents of fluorite in the Yama fluorite deposit are basically positively correlated with  $\Sigma$ REE contents (Figure 12a), and the Y/Ho ratios of fluorite from both types of fluorite ores have a comparably invariable range of 41.43–73.79. Apparently, fluorites from the Yama fluorite deposit or their origins of ore-forming fluids follow a recrystallization trend,

indicating an identical fluid origin (Figure 12b; e.g., [58]). Furthermore, hydrothermal fluorites are identified by their high Y/Ho ratios (average between 35 and 250; e.g., [58]). The Y/Ho ratio range of 41.43–73.79 for the studied fluorite samples is much higher than the chondrite Y/Ho ratio [63], PAAS Y/Ho ratio [47], and most igneous rocks [58], and is located within the Y/Ho value range of hydrothermal fluorites (Figure 12c) [58], suggesting that the fluorites in the Yama fluorite deposit might be derived from a hydrothermal source rather than the surrounding syenogranites. Moreover, fluorites in the study area showing positive Y anomalies also suggested that Y enrichment depends on the presence of Y–F complexes (e.g., [64]), which have a higher stability when compared with Ho–F complexes [65]. Therefore, Y preferentially stays within the fluorite formed from F-rich fluids.

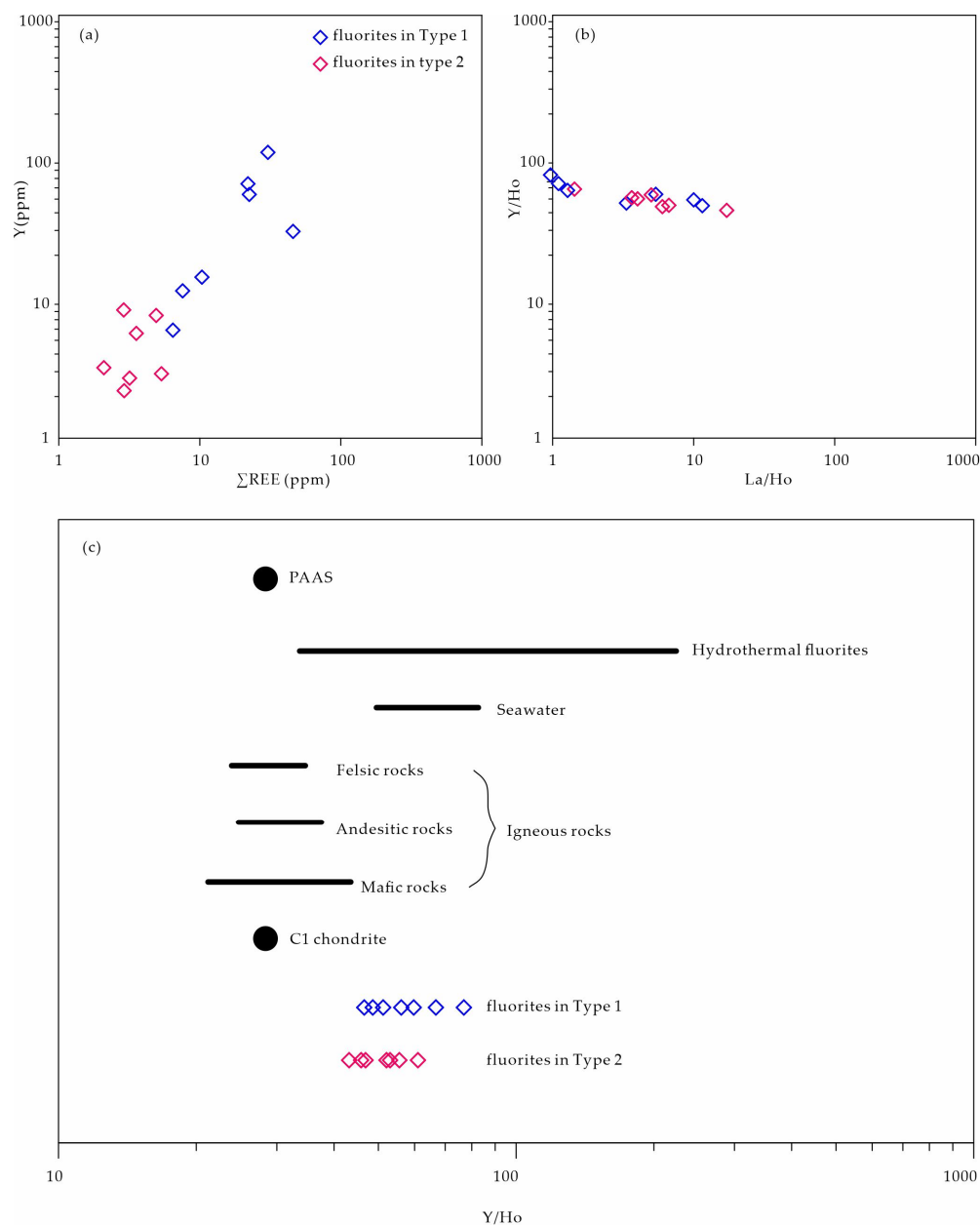


**Figure 12.** Plot of (a) Y versus ΣREEs and (b) Y/Ho versus La/Ho for fluorites from the Yama deposit; (c) comparison of the Y/Ho ratios of fluorites from the Yama deposit. Igneous rocks and hydrothermal fluorite are also plotted for comparison (after [58]). PAAS data were obtained from [47], and C1 chondrite data were obtained from [63].



The valence state of Eu in fluorite and the Eu anomalies relative to other REEs can reveal the redox state of the ore-forming fluid [58]. In the reducing environment, some Eu takes on the form of  $\text{Eu}^{2+}$ , and the  $\text{Eu}^{2+}$  ionic radius is large and cannot easily replace  $\text{Ca}^{2+}$ , thus forming a negative Eu anomaly [66]. There were weak to moderate negative Eu anomalies ( $\text{Eu}/\text{Eu}^* = 0.16\text{--}0.40$ ) of fluorite in the Yama fluorite deposit; therefore,  $\text{Eu}^{2+}$  should exist in the fluorite in the Yama fluorite deposit and indicate a reducing environment. These negative Eu anomalies indicate the low O fugacity conditions of the hydrothermal fluids (e.g., [67–69]).

To obtain a precise ore-forming age for fluorite mineralization in the Yama fluorite deposit, we attempted to carry out the Sm-Nd isotope analysis of five fluorite samples. However, we did not obtain reliable Sm-Nd isotope data for our samples, as well as an isochron age. Fluorite mineralization is a type of hydrothermal filling of fluorite–quartz veins in the Yama fluorite deposit, and no coeval hydrothermal alterations can be observed close to the quartz–fluorite veins within the syenogranite wall rocks. According to the above geological fact, it was indicated that there is very weak fluid–rock interactions between ore-forming meteoric fluid and surrounding syenogranites during fluorite and quartz filling. Therefore, the ore-forming age for fluorite mineralization should be later than the forming age of syenogranite wall rocks (i.e., mean age = 443 Ma [10]).

Commonly, the Late Ordovician–Early Silurian syenogranites in the study area were considered to be emplaced in a post-collisional setting which was related to the closure of the South Qilian Ocean (a branch of the Proto-Tethys Ocean) between the Qaidam Block and SQB [10]. Since the occurrence of such numerous Early Paleozoic granitic emplacements, subsequent dominant tectonic and magmatic activities within the SQB had happened predominantly in the Permian–Triassic and were considered to be closely related to the evolution of the Paleo-Tethys Ocean between the QM and the SQB [6]. Therefore, we assume that the meteoric water under the Yama area was possibly heated and convected in the Permian–Triassic, and then might be turned into a type of reduced, low-temperature, F-bearing hydrothermal fluid which might extract F from the deep surrounding rocks. The late, large-scale brittle faults within the Late Ordovician–Early Silurian syenogranites in the Yama area would provide a wide space for migration pathways and the rapid filling of F-bearing ore-forming fluids. Finally, quartz veins and quartz–fluorite veins filled along faults within the syenogranite wall rocks in the Yama area. In essence, the Yama fluorite deposit is a fault-controlled hydrothermal vein-type deposit (e.g., [70,71]), and might be also classified as a Qiquanba type of meso-epithermal fluorite deposit in China, as proposed by [72]. The Late Ordovician–Early Silurian syenogranites as well as other granites in the Tataleng granitic batholith are just wall rocks for fluorite mineralization; thus, potential fluorite mineralization should be searched for within the subsidiary brittle faults within granites rather than in the granitic bodies themselves.

## 6. Conclusions

Petrographic observation; H, O, and Sr isotope analyses; and trace element and REE analyses were conducted on fluorites within the quartz–fluorite veins in the Yama fluorite deposit in the Tataleng granitic batholith in the SQB. Based on these analyses, the following conclusions can be drawn:

- (1) The paragenetic sequences for the Yama fluorite mineralization can be divided into two major stages, i.e., the pre-ore quartz stage, and the hydrothermal stage, and the latter stage can be subdivided into the quartz–fluorite epoch and the quartz–calcite epoch. Fluorite-free quartz veins, fluorite–quartz veins, and a few quartz–calcite veins were formed in the pre-ore stage, the quartz–fluorite epoch, and the quartz–calcite epoch, respectively. Typical fluorite–quartz veins consist of Type 1 fluorite ores showing vein structures, veinlet, stringer structures, and/or pectinate, and Type 2 ores showing breccia structures within veins.
- (2) Fluorite samples from fluorite–quartz veins have roughly similar REY patterns with relatively strong enrichment in HREEs, negative Eu anomalies ( $\text{Eu}/\text{Eu}^* = 0.16\text{--}0.40$ ),

strongly positive Y anomalies ( $Y/Y^* = 1.43\text{--}2.39$ ), relatively high  $(La/Yb)_N$  values of 0.69–8.43, and comparably invariable range Y/Ho ratios (41.43–73.79), suggesting a reduced hydrothermal genesis.

- (3) Fluorites in two types of fluorite ore have relatively variable  $\delta D$  and  $\delta^{18}O$  values of  $-77.4\text{‰}$  to  $-102.4\text{‰}$  and  $-12.7\text{‰}$  to  $-4.3\text{‰}$ , respectively, and the  $\delta D$  value ranges of two types of fluorite ores roughly overlap each other; however, Type 2 samples show slightly heavier  $\delta^{18}O$  values than Type 1, suggesting the origin of the ore-forming fluid for the Yama fluorite mineralization might predominantly originate from paleo-meteoric water, and a mixture with certain deep water sources (e.g., magmatic water or metamorphic water) cannot also be totally precluded.
- (4) Two types of fluorites have a relatively invariable range of 0.749089–0.756628 except an anomalously high ratio of 0.828185, and the syenogranite wall rocks have variable analytical  $^{87}Sr/^{86}Sr$  ratios of 0.832625–1.191950. The calculated initial  $^{87}Sr/^{86}Sr$  ratios of fluorites based on given ore-forming ages less than 443 Ma are apparently higher than the initial  $^{87}Sr/^{86}Sr$  ratios of syenogranites, indicating the Sr source should be predominantly derived from the ore-forming fluids themselves rather than from the syenogranite wall rocks.
- (5) Combining the geological characteristics, trace element and REE geochemistry, and the isotope (H, O, and Sr) geochemistry, it was suggested that the Yama fluorite deposit can be classified as a fault-controlled hydrothermal vein-type deposit, and ore-forming water and materials might be directly derived from the evolutionary meteoric water rather than syenogranite wall rocks. The late large-scale faults within the Late Ordovician–Early Silurian syenogranites in the Yama area would provide a wide space for migration pathways and rapid filling of F-bearing ore-forming fluids. Finally, quartz veins and quartz–fluorite veins are filled alongside them, and weak hydrothermal alterations can be observed close to the veins within syenogranite wall rocks.

**Author Contributions:** Author Contributions: Conceptualization, Q.-F.D.; methodology, H.J., X.Z. and R.-Z.W.; software, X.Z. and R.-Z.W.; validation, H.J., Q.-F.D. and R.-Z.W.; formal analysis, H.J., X.Z., R.-Z.W. and Q.-F.D.; investigation, H.J., R.-Z.W., X.Z., G.-B.H., W.M., Q.-Q.C., W.-H.W. and Q.-F.D.; resources, H.J., G.-B.H., Q.-Q.C. and Q.-F.D.; data curation, H.J. and Q.-F.D.; writing—original draft preparation, H.J. and Q.-F.D.; writing—review and editing, H.J. and Q.-F.D.; visualization, H.J., X.Z. and Q.-F.D.; supervision, Q.-F.D.; project administration, H.J. and Q.-F.D.; funding acquisition, H.J. and Q.-F.D. All authors have read and agreed to the published version of the manuscript.

**Funding:** This research was funded by the First Group of Geological Survey Project in 2024 from the Bureau of Geological Exploration & Development of Qinghai Province, grant number: File (2023) 50.

**Data Availability Statement:** The datasets generated during and/or analyzed during the current study are available in full within the published article.

**Acknowledgments:** We are grateful to the analytical Laboratories at ALS Chemex (Guangzhou, China) Co., Ltd., BRIUG, and BCTT for their help with the element and stable isotope analyses. We also thank the three reviewers for their thoughtful reviews.

**Conflicts of Interest:** The authors declare no conflict of interest.

## References

1. Xiao, W.; Windley, B.F.; Yong, Y.; Yan, Z.; Yuan, C.; Liu, C.; Li, J. Early Paleozoic to Devonian multiple-accretionary model for the Qilian Shan, NW China. *J. Asian Earth Sci.* **2009**, *35*, 323–333. [[CrossRef](#)]
2. Song, S.; Niu, Y.; Su, L.; Xia, X. Tectonics of the North Qilian orogen, NW China. *Gondwana Res.* **2013**, *23*, 1378–1401. [[CrossRef](#)]
3. Song, S.; Niu, Y.; Su, L.; Zhang, C.; Zhang, L. Continental orogenesis from ocean subduction, continent collision/subduction, to orogen collapse, and orogen recycling: The example of the North Qaidam UHPM belt, NW China. *Earth-Sci. Rev.* **2014**, *129*, 59–84. [[CrossRef](#)]
4. Wang, C.; Li, R.; Smithies, R.H.; Li, M.; Peng, Y.; Chen, F.; He, S. Early Paleozoic felsic magmatic evolution of the western Central Qilian belt, Northwestern China, and constraints on convergent margin processes. *Gondwana Res.* **2017**, *41*, 301–324. [[CrossRef](#)]

5. Yan, Z.; Fu, C.; Aitchison, J.C.; Buckman, S.; Niu, M.; Cao, B.; Sun, Y.; Guo, X.; Wang, Z.; Zhou, R. Retro-foreland Basin Development in Response to Proto-Tethyan Ocean Closure, NE Tibet Plateau. *Tectonics* **2019**, *38*, 4229–4248. [[CrossRef](#)]
6. Ding, Q.F.; Pan, T.; Zhou, X.; Cheng, L.; Li, S.P.; Han, J.; Qian, Y.; Gao, Y.; Shang, M.Y. Geochronology, petrogenesis, and tectonic significance of the granites in the Chaqiabeishan area of the Quanji Massif, northwestern China. *Geol. J.* **2022**, *57*, 1241–1261. [[CrossRef](#)]
7. Song, S.; Yang, L.; Zhang, Y.; Niu, Y.; Wang, C.; Su, L.; Gao, Y. Qi-Qin Accretionary Belt in Central China Orogen: Accretion by trench jam of oceanic plateau and formation of intra-oceanic arc in the Early Paleozoic Qin-Qi-Kun Ocean. *Sci. Bull.* **2017**, *62*, 1035–1038. [[CrossRef](#)]
8. Sun, Y.; Niu, M.; Li, X.; Wu, Q.; Cai, Q.; Yuan, X.; Li, C. Petrogenesis and tectonic implications from the Ayishan Group in the South Qilian Belt, NW China. *Geol. J.* **2020**, *55*, 6860–6877. [[CrossRef](#)]
9. He, X.; Fu, C.; Yan, Z.; Wang, B.; Niu, M.; Li, X. Petrogenesis and tectonic implication of the lower Silurian high-Sr/Y subvolcanic rocks from the South Qilian suture zone in the Qilian Orogen, NW China. *Geol. Mag.* **2021**, *158*, 1383–1402. [[CrossRef](#)]
10. Jiao, H.; Lu, H.; Huang, G.; Cui, Q.; Ding, Q.; Zhou, X.; Wu, R. Geochronology, petrogenesis, and mineralization potential of the syenogranites in the Yama fluorite deposit, Tataleng granitic batholith, Qilian Orogen, NW China. *Can. J. Earth Sci.* **2023**, *60*, 1647–1673. [[CrossRef](#)]
11. Wu, C.L.; Yang, J.S.; Wooden, J.L.; Liou, J.G.; Li, H.B.; Meng, F.C.; Persing, H.; Meibom, A. Zircon SHRIMP dating of granite from Qaidamshan, NW China. *Chin. Sci. Bull.* **2002**, *47*, 418–422. [[CrossRef](#)]
12. Tseng, C.; Yang, H.; Yang, H.; Liu, D.; Wu, C.; Cheng, C.; Chen, C.; Ker, C. Continuity of the North Qilian and North Qinling orogenic belts, Central Orogenic System of China: Evidence from newly discovered Paleozoic adakitic rocks. *Gondwana Res.* **2009**, *16*, 285–293. [[CrossRef](#)]
13. Chen, Y.; Song, S.; Niu, Y.; Wei, C. Melting of continental crust during subduction initiation: A case study from the Chaidanuo peraluminous granite in the North Qilian suture zone. *Geochim. Cosmochim. Acta* **2014**, *132*, 311–336. [[CrossRef](#)]
14. Yang, H.; Zhang, H.; Luo, B.; Zhang, J.; Xiong, Z.; Guo, L.; Pan, F. Early Paleozoic intrusive rocks from the eastern Qilian orogen, NE Tibetan Plateau: Petrogenesis and tectonic significance. *Lithos* **2015**, *224–225*, 13–31. [[CrossRef](#)]
15. Yu, S.; Zhang, J.; Qin, H.; Sun, D.; Zhao, X.; Cong, F.; Li, Y. Petrogenesis of the early Paleozoic low-Mg and high-Mg adakitic rocks in the North Qilian orogenic belt, NW China: Implications for transition from crustal thickening to extension thinning. *J. Asian Earth Sci.* **2015**, *107*, 122–139. [[CrossRef](#)]
16. Tung, K.; Yang, H.; Yang, H.; Smith, A.; Liu, D.; Zhang, J.; Wu, C.; Shau, Y.; Wen, D.; Tseng, C. Magma sources and petrogenesis of the early–middle Paleozoic backarc granitoids from the central part of the Qilian block, NW China. *Gondwana Res.* **2016**, *38*, 197–219. [[CrossRef](#)]
17. Yang, H.; Zhang, H.; Xiao, W.; Tao, L.; Gao, Z.; Luo, B.; Zhang, L. Multiple Early Paleozoic granitoids from the southeastern Qilian orogen, NW China: Magma responses to slab roll-back and break-off. *Lithos* **2021**, *380–381*, 105910. [[CrossRef](#)]
18. Li, J.; Xia, Y.; Jiang, H.; Zhang, X.; Zhang, X.; Wang, Y.; Lei, T.; Liu, Y. Magma hybridization and crust-mantle interaction revealed by mineralogical and geochemical footprints: A case study from the South Qilian Accretionary Belt at the northern Tibetan Plateau. *Int. Geol. Rev.* **2021**, *64*, 2284–2305. [[CrossRef](#)]
19. Zhao, J.; Wu, B.; Zhang, X.; Chen, W.; Ma, X. Petrogenesis of Early Paleozoic adakitic granitoids in the eastern Qilian Block, northwest China: Implications for the South Qilian Ocean subduction. *Mineral. Petrol.* **2021**, *115*, 687–708. [[CrossRef](#)]
20. Zhu, X.; Chen, D.; Ren, Y.; Yang, M.; Wang, C. Late Silurian mafic and felsic magmatism in the South Qilian Belt, northern Tibet Plateau: Response to slab breakoff. *Lithos* **2021**, *380*, 105860. [[CrossRef](#)]
21. Zhang, B.W. Study on Metalliferous Deposits Mineralization in Southern Qilian Orogenic Belt, Qinghai Province. Ph.D. Thesis, Jilin University, Changchun, China, 2010.
22. Li, S.J. Geodynamic Evolution of Qilian Orogenic Belt and Metallogensis of Endogenous Metals. Ph.D. Thesis, Jilin University, Changchun, China, 2011.
23. Li, S.J.; Zeng, X.P.; Wang, F.C.; Tong, H.K.; Yang, Y.Q.; Zhang, D.X.; Kang, B.; Shi, H.Y.; Zheng, Z.H. Main metallogenic series and prospecting potential in Qinghai province. *J. Jilin Univ. (Earth Sci. Ed.)* **2022**, *52*, 1419–1445. [[CrossRef](#)]
24. QIGEIQP. *Interim Report of Geological Survey for Fluorite Mineralizations in Yama Area in Delingha City, Qinghai Province*; Qaidam Integrated Geological Exploration Institute of Qinghai Province (QIGEIQP): Golmud, China, 2023.
25. Yan, Z.; Fu, C.; Aitchison, J.C.; Niu, M.; Buckman, S.; Cao, B. Early Cambrian Muli arc–ophiolite complex: A relic of the Proto-Tethys oceanic lithosphere in the Qilian Orogen, NW China. *Int. J. Earth Sci. (Geol. Rundsch.)* **2019**, *108*, 1147–1164. [[CrossRef](#)]
26. Fu, C.; Yan, Z.; Wang, Z.; Buckman, S.; Aitchison, J.C.; Niu, M.; Cao, B.; Guo, X.; Li, X.; Li, Y.; et al. Lajishankou Ophiolite Complex: Implications for Paleozoic Multiple Accretionary and Collisional Events in the South Qilian Belt. *Tectonics* **2018**, *37*, 1321–1346. [[CrossRef](#)]
27. Kang, H.; Chen, Y.; Li, D. The nature and history of the South Qilian orogenic belt: Constraints from compositions of rivers’ sediments and their detrital zircon U-Pb geochronology, Lu-Hf isotopic compositions. *Geol. J.* **2020**, *55*, 712–727. [[CrossRef](#)]
28. Wang, D.; Wang, T.; Yan, J.; Lin, X. Petrogenesis and tectonic implications of early Palaeozoic igneous rocks of the western South Qilian Belt, central China. *Int. Geol. Rev.* **2018**, *60*, 844–864. [[CrossRef](#)]
29. Tung, K.; Yang, H.; Yang, H.; Liu, D.; Zhang, J.; Wan, Y.; Tseng, C. SHRIMP U-Pb geochronology of the zircons from the Precambrian basement of the Qilian Block and its geological significances. *Chin. Sci. Bull.* **2007**, *52*, 2687–2701. [[CrossRef](#)]

30. Xu, Z.Q.; Xu, H.F.; Zhang, J.X.; Li, H.B.; Zhu, Z.Z.; Qu, J.C.; Chen, D.N.; Chen, J.L.; Yang, K.C. The Zoulang Nanshan Caledonian subduction complex in the Northern Qilian Mountains and its dynamics1. *Acta Geol. Sin.* **1994**, *7*, 241.
31. Feng, Y.M.; He, S.P. *Geotectonics and Orogeny of the Qilian Mountains*; Geological Publish House: Beijing, China, 1996; p. 721.
32. Wu, C.L.; Yang, J.S.; Wooden, J.; Liou, J.G.; Li, H.B.; Meng, F.C.; Persing, H.; Meibom, A. Zircon SHRIMP dating for the Qaidam mountain granite. *Sci. Bull.* **2001**, *46*, 1743–1747. (In Chinese)
33. Hu, G.N.; Wang, R.; Wang, X.X.; Sun, Y.G.; Lin, W.; Shen, W.H. Mineralogical characteristics and petrological significance of the Tataleng Rapakivi granite in the Northern margin of the Qaidam basin. *J. Earth Sci. Environ.* **2008**, *30*, 337–345. (In Chinese with English Abstract)
34. Zhou, B.; Zheng, Y.Y.; Xu, R.K.; Wang, Y.K.; Zhang, X.P.; Wu, L. LA-ICP-MS zircon U-Pb dating and Hf isotope geochemical characteristics of Qaidamshan intrusive body. *Geol. Bull. China* **2013**, *32*, 1027–1034. (In Chinese with English Abstract)
35. Zhu, X.H.; Wang, H.L.; Yang, M. Zircon U–Pb age of the monzogranite from the middle segment of the Qaidam Mountain composite granite on the South margin of the Qilian mountain. *Geol. China* **2016**, *43*, 751–767. (In Chinese with English Abstract)
36. He, X.Y.; Wang, Y.; Guo, R.H. Petrology, geochemistry, and zircon U-Pb geochronology of the Chaidamu mountain granite. *Geol. Rev.* **2019**, *65*, 55–56. (In Chinese)
37. He, X.Y.; Yang, X.K.; Wang, Y.; Guo, R.H.; Liao, Y.Y.; Fan, F.H. Petrology, geochemistry, and zircon U-Pb geochronology of the Chaidamushan granite from the southern margin of Qilianshan. *Acta Geol. Sin.* **2020**, *94*, 1248–1263. (In Chinese with English Abstract)
38. Huang, H.; Niu, Y.; Nowell, G.; Zhao, Z.; Yu, X.; Mo, X. The nature and history of the Qilian Block in the context of the development of the Greater Tibetan Plateau. *Gondwana Res.* **2015**, *28*, 209–224. [[CrossRef](#)]
39. Wang, Q.; Dong, Y.; Pan, Y.; Liao, F.; Guo, X. Early Paleozoic Granulite-Facies Metamorphism and Magmatism in the Northern Wulan Terrane of the Quanji Massif: Implications for the Evolution of the Proto-Tethys Ocean in Northwestern China. *J. Earth Sci.* **2018**, *29*, 1081–1101. [[CrossRef](#)]
40. Wu, C.L.; Wooden, J.L.; Mazadab, F.K.; Mattinson, C.; Gao, Y.H.; Wu, S.P.; Chen, Q.L. Zircon SHRIMP U-Pb dating of granites from the Da Qaidam area in the north margin of Qaidam basin, NW China. *Acta Petrol. Sin.* **2007**, *23*, 1861–1875. (In Chinese with English abstract)
41. Lu, X.X.; Sun, Y.G.; Zhang, X.T.; Xiao, Q.H.; Wang, X.X.; Wei, X.D.; Gu, D.M. The SHRIMP age of Tataleng Rapakivi granite at the north margin of Qaidam basin. *Acta Geol. Sin.* **2007**, *81*, 626–634. (In Chinese with English Abstract)
42. Clayton, R.N.; Mayeda, T.K. The use of bromine pentafluoride in the extraction of oxygen from oxides and silicates for isotopic analysis. *Geochim. Cosmochim. Acta* **1963**, *27*, 43–52. [[CrossRef](#)]
43. Clayton, R.N.; O’Neil, J.R.; Mayeda, T.K. Oxygen isotope exchange between quartz and water. *J. Geophys. Res.* **1972**, *77*, 3057–3067. [[CrossRef](#)]
44. Liu, H.B.; Jin, G.S.; Li, J.J.; Han, J.; Zhang, J.F.; Zhang, J.; Zhong, F.W.; Guo, D.Q. Determination of stable isotope composition in uranium geological samples. *World Nucl. Geosci.* **2013**, *30*, 174–179. (In Chinese with English Abstract)
45. Yang, Y.; Zhang, H.; Chu, Z.; Xie, L.; Wu, F. Combined chemical separation of Lu, Hf, Rb, Sr, Sm and Nd from a single rock digest and precise and accurate isotope determinations of Lu–Hf, Rb–Sr and Sm–Nd isotope systems using Multi-Collector ICP-MS and TIMS. *Int. J. Mass Spectrom.* **2010**, *290*, 120–126. [[CrossRef](#)]
46. Boynton, W.V. *Geochemistry of the Rare Earth Elements: Meteorites Studies*; Elsevier: New York, NY, USA, 1984; pp. 63–114.
47. Taylor, S.R.; McLennan, S.M. *The Continental Crust: Its Composition and Evolution*; Blackwell: Oxford, UK, 1985; p. 312.
48. Goldfarb, R.J.; Ayuso, R.; Miller, M.L.; Ebert, S.W.; Marsh, E.E.; Petsel, S.A.; Miller, L.D.; Bradley, D.C.; Johnson, C.; McClelland, W. The Late Cretaceous Donlin Creek gold deposit, Southwestern Alaska: Controls on epizonal ore formation. *Econ. Geol.* **2004**, *99*, 643–671. [[CrossRef](#)]
49. Sheppard, S. Characterization and isotopic variations in natural waters. *Rev. Mineral. Geochem.* **1986**, *16*, 165–183. [[CrossRef](#)]
50. Steiger, R.H.; Jäger, E. Subcommittee on geochronology: Convention on the use of decay constants in geo- and cosmochronology. *Earth Planet. Sci. Lett.* **1977**, *36*, 359–362. [[CrossRef](#)]
51. Pei, Q.; Li, C.; Zhang, S.; Zou, H.; Liang, Y.; Wang, L.; Li, S.; Cao, H. Vein-type fluorite mineralization of the Linxi district in the Great Xing’an Range, Northeast China: Insights from geochronology, mineral geochemistry, fluid inclusion and stable isotope systematics. *Ore Geol. Rev.* **2022**, *142*, 104708. [[CrossRef](#)]
52. Craig, H. The isotopic composition of water and carbon in geothermal areas. In *Nuclear Geology on Geothermal Areas*; Tongiorgi, E., Ed.; CNR Laboratorio di Geologia Nucleare: Pisa, Italy, 1963; pp. 17–53.
53. Goldfarb, R.J.; Snee, L.W.; Miller, L.D.; Newberry, R.J. Rapid dewatering of the crust deduced from ages of mesothermal gold deposits. *Nature* **1991**, *354*, 296–298. [[CrossRef](#)]
54. Jiang, S.H.; Nie, F.J.; Hu, P.; Lai, X.R.; Liu, Y.F. Mayum: An orogenic gold deposit in Tibet, China. *Ore Geol. Rev.* **2009**, *36*, 160–173. [[CrossRef](#)]
55. McCuaig, C.T.; Kerrich, R. P–T–Deformation—Fluid characteristics of lode gold deposits: Evidence from alteration systematics. *Ore Geol. Rev.* **1998**, *12*, 381–453. [[CrossRef](#)]
56. Möller, P.; Parekh, P.P.; Schneider, H.J. The Application of Tb/Ca–Tb/La Abundance Ratios to Problems of Fluorspar Genesis. *Miner. Depos.* **1976**, *11*, 111–116. [[CrossRef](#)]
57. Barbieri, M.; Tolomeo, L.; Voltaggio, M. Yttrium, lanthanum and Manganese geochemistry in fluorite deposits from Sardinia (Italy). *Chem. Geol.* **1983**, *40*, 43–50. [[CrossRef](#)]



58. Bau, M.; Dulski, P. Comparative study of yttrium and rare-earth element behaviours in fluorine-rich hydrothermal fluids. *Contrib. Mineral. Petrol.* **1995**, *119*, 213–223. [[CrossRef](#)]
59. Ye, X.; Bai, F. Spectral characteristics, rare earth elements, and ore-forming fluid constrains on the origin of fluorite deposit in Nanlishu, Jilin Province, China. *Minerals* **2022**, *12*, 1195. [[CrossRef](#)]
60. Singh, T.; Upadhyay, D.; Patel, A.K.; Mishra, B. High MREE-HREE solubility in a carbonatite-derived hydrothermal fluid: Evidence from fluorite-hosted fluid inclusions in the Amba Dongar carbonatite complex, India. *Chem. Geol.* **2022**, *613*, 121162. [[CrossRef](#)]
61. Liu, B.; Wu, Q.; Li, H.; Wu, J.; Cao, J.; Jiang, J.; Liang, W. Fault-controlled fluid evolution in the Xitian W-Sn-Pb-Zn-fluorite mineralization system (South China): Insights from fluorite texture, geochemistry and geochronology. *Ore Geol. Rev.* **2020**, *116*, 103233. [[CrossRef](#)]
62. Irber, W. The lanthanide tetrad effect and its correlation with K/Rb, Eu/Eu\*, Sr/Eu, Y/Ho, and Zr/Hf of evolving peraluminous granite suites. *Geochim. Cosmochim. Acta* **1999**, *63*, 489–508. [[CrossRef](#)]
63. Anders, E.; Grevesse, N. Abundances of the elements: Meteoritic and solar. *Geochim. Cosmochim. Acta* **1989**, *53*, 197–214. [[CrossRef](#)]
64. Möller, P. Europium anomalies in hydrothermal minerals. Kinetic versus thermodynamic interpretation. In Proceedings of the Ninth Quadrennial IAGOD Symposium, Beijing, China, 12–18 August 1994; Schweizerbart: Stuttgart, Germany, 1998; pp. 239–246.
65. Bau, M. Controls on the fractionation of isovalent trace elements in magmatic and aqueous systems: Evidence from Y/Ho, Zr/Hf, and lanthanide tetrad effect. *Contrib. Mineral. Petrol.* **1996**, *123*, 323–333. [[CrossRef](#)]
66. Möller, P. REE fractionation in hydrothermal fluorite and calcite. In *Source, Transport and Deposition of Metals*, 1st ed.; Pagel, M., Leroy, J.L., Eds.; Balkema: Rotterdam, The Netherlands, 1991; pp. 91–94.
67. Sasmaz, A.; Yavuz, F.; Sagioglu, A.; Akgul, B. Geochemical patterns of the Akdagmadeni (Yozgat, Central Turkey) fluorite deposits and implications. *J. Asian Earth Sci.* **2005**, *24*, 469–479. [[CrossRef](#)]
68. Sasmaz, A.; Kryuchenko, N.; Zhovinsky, E.; Suyarko, V.; Konakci, N.; Akgul, B. Major, trace and rare earth element (REE) geochemistry of different colored fluorites in the Bobrynets region, Ukraine. *Ore Geol. Rev.* **2018**, *102*, 338–350. [[CrossRef](#)]
69. Duan, Z.; Jiang, S.; Su, H.; Zhu, X.; Zou, T.; Cheng, X. Trace and Rare Earth Elements, and Sr Isotopic Compositions of Fluorite from the Shihuiyao Rare Metal Deposit, Inner Mongolia: Implication for Its Origin. *Minerals* **2020**, *10*, 882. [[CrossRef](#)]
70. Zhao, Y.; Pei, Q.; Zhang, S.; Guo, G.; Li, J.; Liu, W.; Hu, X.; Song, K.; Wang, L. Formation timing and genesis of Madiu fluorite deposit in East Qinling, China: Constraints from fluid inclusion, geochemistry, and H–O–Sr–Nd isotopes. *Geol. J.* **2020**, *55*, 2532–2549. [[CrossRef](#)]
71. Pei, Q.; Zhang, S.; Hayashi, K.; Wang, L.; Cao, H.; Zhao, Y.; Hu, X.; Song, K.; Chao, W. Nature and Genesis of the Xiaobeigou Fluorite Deposit, Inner Mongolia, Northeast China: Evidence from Fluid Inclusions and Stable Isotopes. *Resour. Geol.* **2019**, *69*, 148–166. [[CrossRef](#)]
72. Han, B.; Shang, P.; Gao, Y.; Jiao, S.; Yao, C.; Zou, H.; Li, M.; Wang, L.; Zheng, H. Fluorite deposits in China: Geological features, metallogenic regularity, and research progress. *China Geol.* **2020**, *3*, 473–489.

**Disclaimer/Publisher’s Note:** The statements, opinions and data contained in all publications are solely those of the individual author(s) and contributor(s) and not of MDPI and/or the editor(s). MDPI and/or the editor(s) disclaim responsibility for any injury to people or property resulting from any ideas, methods, instructions or products referred to in the content.